

1 Running title: Loss of synchronized intra-islet Ca<sup>2+</sup> oscillations *in vivo* in *Robo*-deficient  $\beta$  cells

2

3 **Synchronized  $\beta$  cell response to glucose is lost concomitant with loss of islet architecture in**

4 ***Robo* deficient islets of Langerhans *in vivo***

5

6 Melissa T. Adams<sup>1</sup>, Christopher A. Reissaus<sup>2</sup>, JaeAnn M. Dwulet<sup>3</sup>, Erli Jin<sup>4</sup>, Joseph M.

7 Szulczewski<sup>1</sup>, Melissa R. Lyman<sup>1</sup>, Sophia M. Sdao<sup>4</sup>, Sutichot D. Nimkulrat<sup>1</sup>, Suzanne M. Ponik<sup>1</sup>,

8 Matthew J. Merrins<sup>4</sup>, Richard K.P. Benninger<sup>3</sup>, Raghavendra G. Mirmira<sup>5</sup>, Amelia K. Linnemann<sup>2</sup>,

9 Barak Blum<sup>1\*</sup>

10

11 <sup>1</sup>Department of Cell and Regenerative Biology, University of Wisconsin-Madison, Madison, WI  
12 53705, USA

13 <sup>2</sup>Herman B Wells Center for Pediatric Research and Center for Diabetes and Metabolic Diseases,  
14 Indiana University School of Medicine, Indianapolis, IN 46202, USA

15 <sup>3</sup>Department of Bioengineering and Barbara Davis Center for Diabetes, University of Colorado  
16 Denver, Anschutz Medical Campus, Aurora, CO. 80045, USA

17 <sup>4</sup>Department of Medicine, Division of Endocrinology, Diabetes, and Metabolism, University of  
18 Wisconsin-Madison, Madison, Wisconsin 53705, USA

19 <sup>5</sup>Kovler Diabetes Center and the Department of Medicine, University of Chicago, Chicago, IL  
20 60637, USA

21

22 **\*Lead contact and Corresponding Author:** Barak Blum; bblum4@wisc.edu

23 **Abstract**

24 The spatial architecture of the islets of Langerhans is hypothesized to facilitate synchronized  
25 insulin secretion between  $\beta$  cells, yet testing this *in vivo* in the intact pancreas is challenging.  
26 *Robo*  $\beta$ KO mice, in which the genes *Robo1* and *Robo2* are deleted selectively in  $\beta$  cells, provide  
27 a unique model of altered islet spatial architecture without loss of  $\beta$  cell differentiation or islet  
28 damage from diabetes. Combining *Robo*  $\beta$ KO mice with intravital microscopy, we show here  
29 that *Robo*  $\beta$ KO islets lose synchronized intra-islet  $\text{Ca}^{2+}$  oscillations between  $\beta$  cells *in vivo*. We  
30 provide evidence that this loss is not due to a  $\beta$  cell-intrinsic function of Robo, loss of  
31 Connexin36 gap junctions, or changes in islet vascularization, suggesting that the islet  
32 architecture itself is required for synchronized  $\text{Ca}^{2+}$  oscillations. These results have implications  
33 for understanding structure-function relationships in the islets during progression to diabetes  
34 as well as engineering islets from stem cells.

## 35 Introduction

36 The islets of Langerhans, which comprise the endocrine pancreas, are highly organized  
37 micro-organs responsible for maintaining blood glucose homeostasis. Islets are composed of  
38 five endocrine cell types ( $\alpha$ ,  $\beta$ ,  $\delta$ , PP, and  $\epsilon$ ) which, in rodents, are arranged such that the  $\beta$  cells  
39 cluster in the core of the islet, while other non- $\beta$  endocrine cells populate the islet mantle, so  
40 that most  $\beta$  cells are in direct contact preferentially with  $\beta$  cells (homotypic interactions)<sup>1</sup>.  
41 Human islet architecture is more complex and, though its exact organization pattern is still  
42 debated, the prevailing idea is that it still follows a non-random distribution of the different  
43 endocrine cell types<sup>2-6</sup>. In agreement with this notion, computational analysis of human islet  
44 architecture found lower probability of heterotypic interactions and a higher probability of  
45 homotypic interactions between the various endocrine cell types than would be expected if the  
46 islet displayed random distribution of endocrine cells<sup>7,8</sup>. Thus, in both rodent and human islets,  
47 respective stereotypical islet architectures prioritize homotypic over heterotypic interactions  
48 between endocrine cell types<sup>7</sup>. The biological reason for preferential homotypic interactions  
49 between endocrine cells is not completely clear, but it has been suggested to be important for  
50 dictating the level of Connexin36 (Cx36)-mediated electrical  $\beta$  cell- $\beta$  cell coupling, thus allowing  
51 for synchronization of glucose-stimulated insulin secretion (GSIS) between neighboring  $\beta$   
52 cells<sup>9,10</sup>.

53 Activation of insulin secretion in the  $\beta$  cell is triggered when glucose from the blood  
54 enters the  $\beta$  cells through glucose transporters. As this glucose is metabolized, the ratio of  
55 intracellular ATP/ADP in the cells increases. This rise in ATP causes ATP sensitive  $K^+$  channels to  
56 close, resulting in membrane depolarization. The resultant depolarization causes voltage-gated

57  $\text{Ca}^{2+}$  channels to open, triggering an influx of  $\text{Ca}^{2+}$  into the cell, which in turn promotes  
58 exocytosis of insulin granules<sup>11-13</sup>. This chain of events is cyclical and thus results in oscillations  
59 of membrane potential, cytosolic  $\text{Ca}^{2+}$  levels, and insulin secretion in response to glucose<sup>14</sup>.  
60 Because  $\beta$  cells within an islet are gap-junctionally coupled, and thus electrically coupled, these  
61 oscillations are synchronous across all islet  $\beta$  cells<sup>15</sup>. It is thus hypothesized that preferential  $\beta$   
62 cell homotypic contact allows for the necessary amount of gap junctions to form between  
63 neighboring  $\beta$  cells in order to synchronize the oscillations in an entire islet, facilitating pulsatile  
64 insulin secretion<sup>10,16</sup>. Indeed, modeling experiments in which the number of homotypic  $\beta$  cell- $\beta$   
65 cell nearest neighbor connections is lowered within an islet result in predicted perturbation of  
66 synchronous  $\text{Ca}^{2+}$  oscillations<sup>10</sup>. If this *in silico* prediction is correct, then disrupting spatial  
67 organization of the different endocrine cell types within the islet alone, without affecting any  
68 other property of the cells, would be sufficient to disturb synchronized insulin secretion  
69 between  $\beta$  cells. However, direct empirical evidence for this hypothesis is lacking.

70 Most genetic mouse models that show disruption of islet architecture also display  
71 defects in glucose homeostasis<sup>17</sup>. However, in many of these models, the disrupted islet  
72 architecture phenotype is linked to either developmental defects in  $\beta$  cell differentiation or  
73 maturation<sup>18-29</sup> or to pathologies related to  $\beta$  cell damage in diabetes<sup>30-35</sup>. This introduces a  
74 strong confounding factor for studying the role of islet architecture on  $\beta$  cell function.  
75 Therefore, current mouse models of disrupted islet architecture are not suitable for directly  
76 testing the hypothesis that preferential homotypic  $\beta$  cell- $\beta$  cell interactions, dictated by  
77 canonical islet architecture, regulate synchronized insulin secretion between  $\beta$  cells within the  
78 same islet.



79           Recently, we have described a mouse model in which the cell-surface receptors *Robo1*  
80   and *Robo2* are deleted specifically in  $\beta$  cells (*Robo  $\beta$ KO*), resulting in disruption of canonical  
81   endocrine cell type sorting within the islets<sup>36</sup>. Unlike other models of disrupted islet  
82   architecture, the  $\beta$  cells in the islets of *Robo  $\beta$ KO* express normal levels of markers for  $\beta$  cell  
83   differentiation and functional maturity. We reasoned that this model would allow for direct  
84   testing of the role of islet architecture on synchronous islet oscillations between  $\beta$  cells in a fully  
85   differentiated, non-diabetic islet setting.

86

## 87   **Results**

### 88   ***Robo $\beta$ KO* islets have fewer homotypic $\beta$ cell- $\beta$ cell contacts than control islets**

89           *In silico* simulations where the degree of  $\beta$  cell- $\beta$  cell coupling is changed through a  
90   decrease in homotypic nearest neighbors predict that disruption in islet architecture will disrupt  
91   synchronous intra-islet  $\text{Ca}^{2+}$  oscillations and hormone secretion pulses<sup>7,10,37</sup>. To test whether  $\beta$   
92   cells in *Robo  $\beta$ KO* islets have a decreased ratio of homotypic  $\beta$  cell neighbors on average than  
93   control islets, we performed nearest neighbor analysis on islets from pancreatic sections of  
94   *Robo  $\beta$ KO* and control mice (**Figure 1**). We found that *Robo  $\beta$ KO* islets possess significantly  
95   fewer  $\beta$  cell- $\beta$  cell contacts ( $n=9-11$  islets for 3 mice from each genotype; control  $75.35\% \pm 4.1$ ,  
96   *Robo  $\beta$ KO*  $50.37\% \pm 4.1$ ,  $p=0.01$ ), and homotypic contacts in general when compared to control  
97   islets ( $n=9-11$  islets for 3 mice from each genotype; control  $83.7\% \pm 1.7$ , *Robo  $\beta$ KO*  $64.43\% \pm 1.2$ ,  
98    $p=0.0008$ ). We also found that *Robo  $\beta$ KO* islets possess significantly more  $\beta$  cell- $\alpha$  cell contacts  
99   ( $n=9-11$  islets for 3 mice from each genotype; control  $11.21\% \pm 2.7$ , *Robo  $\beta$ KO*  $25.99\% \pm 2.9$ ,  
100    $p=0.02$ ), and heterotypic contacts in general when compared to control islets ( $n=9-11$  islets for

101 3 mice from each genotype; control 16.3%,±1.7 *Robo*  $\beta$ KO 35.57%±1.2,  $p=0.0008$ ). Together,  
102 this suggests that *Robo*  $\beta$ KO islets make fewer homotypic  $\beta$  cell- $\beta$  cell connections compared to  
103 control islets.

104 We have previously shown that genetic deletion of *Robo1* and *Robo2* selectively in  $\beta$   
105 cells using either *Ins1-Cre; Robo1* <sup>$\Delta/\Delta$</sup> *2*<sup>*flx/flx*</sup> or *Ucn3-Cre; Robo1* <sup>$\Delta/\Delta$</sup> *2*<sup>*flx/flx*</sup> mice (*Robo*  $\beta$ KO) results in  
106 disrupted islet architecture and endocrine cell type sorting without affecting  $\beta$  cell death or the  
107 expression of the  $\beta$  cell maturation markers MafA and Ucn3<sup>36</sup>. To verify that  $\beta$  cells in *Robo*  $\beta$ KO  
108 islet are truly mature, we expanded the analysis to look at transcript levels of 15 additional  
109 maturity markers. RNA sequencing and differential gene expression analysis on FACS-purified  $\beta$   
110 cells from both *Robo*  $\beta$ KO and control islets revealed no change in transcript levels of any  
111 hallmark  $\beta$  cell maturity or differentiation genes ( $n=2$  mice of each genotype; **Supplemental**  
112 **Figure 1**). Thus, unlike other mouse models with disrupted islet architecture,  $\beta$  cells in *Robo*  
113  $\beta$ KO islets maintain maturity and differentiation despite loss of normal islet architecture.

114 We reasoned that the altered degree of homotypic  $\beta$  cell- $\beta$  cell interaction in *Robo*  $\beta$ KO  
115 islets together with the seemingly retained  $\beta$  cell maturity provide a unique model by which to  
116 test the hypothesis that endocrine cell type organization affects synchronous insulin secretion  
117 in the islet.

118

### 119 ***Robo* $\beta$ KO islets display unsynchronized Ca<sup>2+</sup> oscillations *in vivo***

120 We set out to investigate how the reduced homotypic  $\beta$  cell- $\beta$  cell connections in *Robo*  
121  $\beta$ KO islets affects dynamic insulin secretion in the islet by measuring dynamic Ca<sup>2+</sup> signaling.  
122 *Robo*  $\beta$ KO islets spontaneously dissociate during isolation and culture<sup>36</sup>, making them

123 unsuitable for *in vitro* analyses of whole-islet  $\text{Ca}^{2+}$  oscillations. To overcome this limitation, we  
124 adopted a novel intravital  $\text{Ca}^{2+}$  imaging method which enables imaging of islet  $\text{Ca}^{2+}$  dynamics *in*  
125 *situ* within the intact pancreas<sup>38</sup>. In brief, this method employs an intravital microscopy (IVM)  
126 platform and adeno-associated viral (AAV) delivery of insulin promoter-driven GCaMP6s, a  
127 fluorescent  $\text{Ca}^{2+}$  biosensor, to quantitate  $\beta$  cell  $\text{Ca}^{2+}$  dynamics *in vivo* in both *Robo*  $\beta$ KO and  
128 control islets. This method also allows for retention of the islet's *in vivo* microenvironment,  
129 blood flow, and innervation, and provides more realistic conditions than *in vitro* approaches  
130 allow for.

131 We verified that synchronous  $\text{Ca}^{2+}$  oscillations are maintained *in vivo* in islets by  
132 measuring GCaMP6s intensity of  $\beta$  cells within AAV8-RIP-GCaMP6 infected islets of control  
133 (*Robo* WT) mice (**Figure 2**). As expected, control mice displayed whole islet synchronous  $\text{Ca}^{2+}$   
134 oscillations when imaged at 0.03, 0.1, and 0.2Hz for at least 10 minutes after glucose elevation  
135 ( $n=8$  islets from 3 mice; **Figure 2** and **Supplemental Video 1 and 2**). We quantified the degree to  
136 which these oscillations are synchronous within the islet by analyzing the amount of correlation  
137 between GCaMP6s active areas within individual islets. While oscillations vary in frequency  
138 between islets, the degree of correlation between  $\beta$  cells within any one islet is very high,  
139 confirming that control islets possess highly synchronous intra-islet  $\text{Ca}^{2+}$  oscillation *in vivo*  
140 (fraction of GCaMP6s active islet area with correlated  $\text{Ca}^{2+}$  oscillations= $0.90\pm 0.04$ ,  $n=8$  islets  
141 from 3 mice; see **Figure 4A**).

142 Conversely, we found that most *Robo*  $\beta$ KO islets display asynchronous intra-islet  $\text{Ca}^{2+}$   
143 oscillations *in vivo* when imaged at 0.03, 0.1, and 0.2Hz (**Figure 3**, **Supplemental Figure 2**,  
144 **Supplemental Videos 3, 4, and 5**). Quantification of this asynchronous behavior through

145 correlation analysis of GCaMP6s activity within individual *Robo*  $\beta$ KO islets revealed significant  
146 reduction in intra-islet correlated oscillation areas compared to controls (fraction of GCaMP6s  
147 activity with correlated  $\text{Ca}^{2+}$  oscillations= $0.58\pm 0.10$ ,  $n= 11$  islets from 5 mice,  $p<0.01$ ; **Figure 4A**).  
148 Further, asynchronous *Robo*  $\beta$ KO islets showed spatially distinct areas within the islet that  
149 oscillated synchronously with immediate  $\beta$  cell neighbors but not with more distant regions  
150 within the same islet (**Figure 3C-D, Supplemental Figure 2, Supplemental Videos 3, 4, and 5**).  
151 This was not due to differences in the proportion of GCaMP6s positive cells showing elevated  
152  $\text{Ca}^{2+}$  activity within *Robo*  $\beta$ KO islets compared to controls (control islets  $0.97\pm 0.01$  fraction  
153 active,  $n=8$  islets from 3 mouse; *Robo*  $\beta$ KO islets  $0.97\pm 0.02$  fraction active,  $n=8$  islets from 4  
154 mice,  $p=0.79$ ; **Figure 4B**).

155

156 ***Unsynchronized  $\text{Ca}^{2+}$  oscillations in *Robo*  $\beta$ KO islets are not due to  $\beta$  cell intrinsic defects in***  
157 ***glucose stimulated  $\text{Ca}^{2+}$  oscillations***

158 *In vitro* experiments have shown that Robo receptors play a role in  $\beta$  cell biology and are  
159 involved in the stimulus secretion cascade linking glucose to insulin secretion<sup>39</sup>. Thus it is  
160 possible that defects in synchronous  $\text{Ca}^{2+}$  oscillations observed in *Robo*  $\beta$ KO islets are due to a  
161 Robo-mediated,  $\beta$  cell-intrinsic effect on dynamic  $\text{Ca}^{2+}$  signaling in response to stimuli.  
162 However, 4 out of the 11 *Robo*  $\beta$ KO islets imaged showed synchronous  $\text{Ca}^{2+}$  activity in greater  
163 than 90% of GCaMP6s positive areas (**Figure 4A, Supplemental Figure 3 and Supplemental**  
164 **video 6**). The existence of this highly synchronous population of *Robo*  $\beta$ KO islets suggests that  
165 the ability of individual  $\beta$  cells to oscillate intracellular  $\text{Ca}^{2+}$  levels in response to stimuli is  
166 unaffected by deletion of *Robo*. Instead, it suggests that islet architecture itself is responsible

167 for controlling synchronized  $\text{Ca}^{2+}$  oscillations, and that some *Robo*  $\beta\text{KO}$  islets may escape this  
168 defect due to less severe architectural disruption. With this in mind, we wanted to test the  
169 extent to which the unsynchronized  $\text{Ca}^{2+}$  oscillations observed in *Robo*  $\beta\text{KO}$  islets *in vivo* are due  
170 to  $\beta$  cell-intrinsic deletion of *Robo per se*.

171 To test whether *Robo*  $\beta\text{KO}$   $\beta$  cells are able to undergo  $\text{Ca}^{2+}$  oscillations in response to  
172 stimuli, we performed *in vitro*  $\text{Ca}^{2+}$  imaging on single  $\beta$  cells from dissociated *Robo*  $\beta\text{KO}$  and  
173 control islets, exposed to glucose followed by KCL (**Figure 5**). We found no difference in the  
174 proportion of  $\beta$  cells that undergo  $\text{Ca}^{2+}$  oscillations in response to 10mM glucose between  
175 control and *Robo*  $\beta\text{KO}$   $\beta$  cells (Control: 70.24% $\pm$ 3.6,  $n=13-32$   $\beta$  cells per mouse for 4 mice, *Robo*  
176  $\beta\text{KO}$ : 61.61% $\pm$ 5.6,  $n=6-24$   $\beta$  cells per mouse for 4 mice,  $p=0.24$ ) (**Figure 5 A-C**). We also saw no  
177 significant difference in area under the curve (AUC) of calcium traces in response to 10mM  
178 glucose (Control: 2.9 $\pm$ 0.17,  $n=13-32$   $\beta$  cells per mouse for 4 mice, *Robo*  $\beta\text{KO}$ : 3.0 $\pm$ 0.21,  $n=6-24$   $\beta$   
179 cells per mouse for 4 mice,  $p=0.39$ )(**Figure 5D**), or peak height of  $\text{Ca}^{2+}$  corresponding to first  
180 phase insulin secretion (Control: 0.34 $\pm$ 0.02,  $n=13-32$   $\beta$  cells per mouse for 4 mice, *Robo*  $\beta\text{KO}$ :  
181 0.41 $\pm$ 0.04,  $n=6-24$   $\beta$  cells per mouse for 4 mice,  $p=0.08$ ) (**Figure 5E**) in *Robo*  $\beta\text{KO}$   $\beta$  cells  
182 compared to controls. There was, however, a significant increase in AUC of  $\text{Ca}^{2+}$  signal in  
183 response to KCL in *Robo*  $\beta\text{KO}$   $\beta$  cells compared to controls (Control: 1.67 $\pm$ 0.07,  $n=13-32$   $\beta$  cells  
184 per mouse for 4 mice, *Robo*  $\beta\text{KO}$ : 2.12 $\pm$ 0.12,  $n=6-24$   $\beta$  cells per mouse for 4 mice,  $p=0.002$ )  
185 (**Figure 5F**), indicating that *Robo*  $\beta\text{KO}$  islets may actually have an increase in magnitude of  $\text{Ca}^{2+}$   
186 response to stimuli. Together, this demonstrates that *Robo*  $\beta\text{KO}$   $\beta$  cells show no defects in their  
187 ability to undergo  $\text{Ca}^{2+}$  oscillations in response to glucose, and in fact may have an improved  
188 stimulus secretion response compared to controls. This is in support of a scenario in which the

189 arrangement of  $\beta$  cells within the islet, rather than a  $\beta$  cell-intrinsic function of Robo, dictates  
190 whole-islet synchronous  $\text{Ca}^{2+}$  oscillations.

191  
192 ***Robo*  $\beta$ KO islets retain the ability to form gap junctions and have similar levels of**  
193 **vascularization**

194 Besides a decrease in  $\beta$  cell- $\beta$  cell homotypic contacts within the islet, a possible  
195 explanation for the loss of synchronized whole islet  $\text{Ca}^{2+}$  oscillations in *Robo*  $\beta$ KO is that their  $\beta$   
196 cells no longer possess the gap junctions necessary for adequate electrical coupling. Indeed, the  
197 phenotype described above is reminiscent of that observed in mice heterozygous for a *Cx36*  
198 null allele<sup>15,40</sup>. To test whether *Robo*  $\beta$ KO mice form fewer gap junctions between  $\beta$  cells, we  
199 measured the area of Cx36 protein immunofluorescence normalized to islet area in *Robo*  $\beta$ KO  
200 and control islets (**Figure 6**). We found no difference in Cx36 immunofluorescence between  
201 *Robo*  $\beta$ KO islets and controls, but significant differences in these two groups compared to *Cx36*  
202 *KO* mice (control islets:  $0.46\% \pm 0.06$  Cx36 signal/ $\mu\text{m}^2$ , *Robo*  $\beta$ KO islets:  $0.69\% \pm 0.11$  Cx36  
203 signal/ $\mu\text{m}^2$ ,  $n=10-15$  islets from 4 mice each,  $p=0.11$ , *Cx36* *KO* islets:  $0.13\% \pm 0.04$ ,  $n=15-20$  islets  
204 from 2 mice) (**Figure 6B**). Furthermore, we found normal co-localization of Cx36 to  $\beta$  cell  
205 borders in both control and *Robo*  $\beta$ KO islets (**Figure 6C**) Overall, this suggests that loss of  
206 synchronous intra-islet  $\text{Ca}^{2+}$  oscillations is not due to failure of gap junction formation in  $\beta$  cells.

207 Another possible explanation for the observed uncoupling of intra-islet  $\text{Ca}^{2+}$  oscillations  
208 in *Robo*  $\beta$ KO islets is that  $\beta$  cell- $\beta$  cell contacts are disrupted due to physical blocking by non-  
209 endocrine tissue. To determine if other non-endocrine architectural changes within the islet  
210 occur in *Robo*  $\beta$ KO mice we quantified the amount of matrix components secreted by vessels as

211 a surrogate for vasculature (laminin, and collagen IV) in *Robo*  $\beta KO$  and control islets. In both  
212 cases we found no significant difference in area of vessel matrix components (**Figure 7**)  
213 between *Robo*  $\beta KO$  and control islets, suggesting that interfering blood vessels are likely not the  
214 cause of loss of whole islet synchronous  $Ca^{2+}$  oscillations (normalized laminin  $\beta 1$  area: control  
215  $0.31 \pm 0.05 \mu m^2$ ,  $n=10-12$  islets from 8 mice; *Robo*  $\beta KO$   $0.38 \pm 0.05 \mu m^2$ ,  $n=10-12$  islets from 8  
216 mice;  $p=0.39$ ; normalized Col IV area: control  $0.18 \pm 0.01 \mu m^2$ ,  $n=10-12$  islets from 4 mice; *Robo*  
217  $\beta KO$   $0.16 \pm 0.02 \mu m^2$ ,  $n=10-12$  islets from 6 mice,  $p=0.35$ ).

218

## 219 Discussion

220 In this study, we provide evidence for the importance of islet architecture for proper  
221 islet function *in vivo*. When islet architecture is disrupted while  $\beta$  cell maturity is retained in  
222 *Robo*  $\beta KO$  mice, synchronized  $Ca^{2+}$  oscillations in the islet *in vivo* are perturbed. This is not due  
223 to a Robo-mediated  $\beta$  cell-intrinsic defect in glucose-stimulated  $Ca^{2+}$  signaling, loss of Cx36, or  
224 change in amount of islet vascularization. *Robo*  $\beta KO$   $\beta$  cells possess a smaller fraction of  
225 homotypic nearest neighbors than controls, suggesting a limited capacity to electrically couple  
226  $\beta$  cells across the islet. Taken together, these data suggest that islet architecture itself,  
227 uncoupled from  $\beta$  cell maturity, Robo-mediated  $\beta$  cell-intrinsic defects in  $Ca^{2+}$  signaling, or  
228 availability of gap junction machinery, is important for coordinated insulin secretion between  $\beta$   
229 cells.

230 Robo, and its ligand Slit, have been previously shown to affect  $Ca^{2+}$  oscillations in  $\beta$  cells  
231 *in vitro*<sup>39</sup>. However, Robo-mediated  $\beta$  cell-intrinsic effects are likely not the cause of  
232 asynchronous *in vivo*  $Ca^{2+}$  oscillations in *Robo*  $\beta KO$  islets. This is supported by two independent

233 observations: 1) single cell  $\text{Ca}^{2+}$  oscillations in dissociated  $\beta$  cells triggered by glucose stimulus *in*  
234 *vitro* are similar between *Robo*  $\beta$ KO and control, and 2) a subset of *Robo*  $\beta$ KO islets analyzed *in*  
235 *vivo* still show synchronized whole-islet  $\text{Ca}^{2+}$  oscillations despite the absence of *Robo*. Further,  
236 this phenotypic heterogeneity is likely not due to an incomplete deletion of *Robo* because all  
237 islets were detected during the  $\text{Ca}^{2+}$  imaging experiment by the fluorescent labeling of  $\beta$  cells  
238 with the H2B-mCherry lineage-tracing reporter<sup>36</sup> which uses the same Cre driver that is used  
239 to delete *Robo* in those  $\beta$  cells. Thus high expression of H2B-mCherry suggests efficient  
240 recombination of the *Robo* floxed allele. All this together supports the idea that *Robo* deletion  
241 in  $\beta$  cells causes disruption of islet architecture, and that this architectural disruption itself  
242 causes loss of synchronized  $\text{Ca}^{2+}$  oscillations. Further, the unsynchronized phenotype in *Robo*  
243  $\beta$ KO islets is clear from the videos we captured at 0.2Hz, 0.1Hz, and 0.03Hz; however we are  
244 aware that even higher imaging frequency may be needed to see asynchronous behavior in  
245 *Robo* WT islets. That said, we note that while faster acquisition would be beneficial to show  
246 more rapid dynamics, we believe it important to capture the dynamics in 3D, in order to ensure  
247 we are not biased by examining certain ‘synchronized regions’ that would not be representative  
248 of the islet dynamics as a whole. We would further argue that the oscillations we observe are  
249 on a 3-5 minute time scale, and therefore to sample these oscillations even at a frequency of 1  
250 frame per 10s of seconds is sufficient. Indeed if we were to image more rapidly and capture  
251 other non-synchronized dynamics in the *Robo*  $\beta$ KO islets, this would reduce the measured  
252 coordination even further. Thus the low sample frequency provides an upper limit to the  
253 coordination.



254 It remains possible that other components of islet architecture besides endocrine cell  
255 type sorting contribute to disruption in  $\text{Ca}^{2+}$  oscillations found in *Robo*  $\beta\text{KO}$  islets. While we  
256 have shown that the amount of vascularization between *Robo*  $\beta\text{KO}$  islets and controls is similar,  
257 we cannot draw conclusions on whether the pattern of vessels is unchanged. Further, it is  
258 possible that the amount and patterning of innervation may vary between *Robo*  $\beta\text{KO}$  and  
259 controls. These are particularly of interest because Robo receptors have known roles in  
260 angiogenesis and axon guidance, and thus could affect precisely how the islet is innervated and  
261 vascularized<sup>41</sup>. Robo also has known roles in controlling cell polarity, and thus it is possible that  
262 this process is disrupted in *Robo*  $\beta\text{KO}$  islets as well. Gap junctions are known to be localized to  
263 the junctional membranes between  $\beta$  cells, which themselves are defined by  $\beta$  cell polarity  
264 within the islet<sup>40,42</sup>. Thus if  $\beta$  cell polarity is disrupted in *Robo*  $\beta\text{KO}$  islets, this could possibly  
265 contribute to the asynchronous  $\text{Ca}^{2+}$  oscillations observed.

266 Finally, while we propose that defects in synchronous  $\text{Ca}^{2+}$  oscillation in response to  
267 glucose in *Robo*  $\beta\text{KO}$  islets are due to inefficient electrical  $\beta$  cell coupling as a result of  
268 decreased homotypic  $\beta$  cell interactions in these islets<sup>43</sup>, we cannot rule out that this effect is  
269 instead due to changes in diffusible paracrine factors. Under this hypothesis, the intermixed  
270 islet architecture that results from deletion of *Robo* in  $\beta$  cells would change the amount and  
271 type of diffusible paracrine signals that endocrine cells within the islet are exposed to. This  
272 change in diffusible factors could affect glucose stimulated insulin secretion and thus could be  
273 contributing to the *in vivo* asynchronous  $\text{Ca}^{2+}$  oscillation phenotype that we observe<sup>44</sup>.

274 **Acknowledgments**

275 We thank Kurt Weiss, Jan Huisken and David Inman for help with imaging. We thank members  
276 of the Blum lab, especially Jennifer Gilbert and Bayley Waters, for valuable discussion. We are  
277 also grateful to Nadav Sharon and Danny Ben-Zvi for critically reading the manuscript. This work  
278 was funded in part by the following grants. R01DK121706, the DRC at Washington University  
279 Pilot Grant P30DK020579, and Pilot Award UL1TR000427 from the UW-Madison Institute for  
280 Clinical and Translational Research (ICTR) to BB; R01DK060581 to RM; R01DK102950 and  
281 R01DK106412 to RKP; R01CA216248 to SP; R01DK113103, R01AG062328, ADA 1-16-IBS-212 to  
282 MM, and an award from the Wisconsin Partnership Program to BB and MM. MTA was funded  
283 by 5T32GM007133-44 and a graduate training award from the UW-Madison Stem Cell &  
284 Regenerative Medicine Center. We also thank the University of Wisconsin Carbone Cancer  
285 Center Support Grant P30CA014520 for use of the UW Flow Core, and the University of  
286 Wisconsin, Madison Biotechnology Center for sequencing and analysis.

287

288 **Author Contribution**

289 Conceptualization, B.B. and M.T.A.; Methodology, B.B., M.T.A., C.A.R., and J.M.D.; Investigation,  
290 M.T.A., C.A.R., J.M.S., M.R.L., S.M.S., E.J., and S.D.N.; Formal Analysis, M.T.A., C.A.R., M.R.L., E.J.,  
291 and J.M.D.; Resources, S.M.P., R.G.M., A.K.L., M.J.M. and R.K.P.B.; Writing Original Draft, B.B. and  
292 M.T.A.; Writing, Review and Editing, all authors; Funding Acquisition, B.B., S.M.P., M.J.M.,  
293 R.K.P.B., R.G.M., and A.K.L.; Supervision, B.B.

## 294 **Materials and Methods**

### 295 **Animals**

296 The experimental protocol for animal usage was reviewed and approved by the University of  
297 Wisconsin-Madison Institutional Animal Care and Use Committee (IACUC) under Protocol  
298 #M005221 and Protocol #M005333, and all animal experiments were conducted in accordance  
299 with the University of Wisconsin-Madison IACUC guidelines under the approved protocol.  
300 *Robo1<sup>Δ</sup>,2<sup>flx45</sup>*, *Ins1-Cre<sup>46</sup>*, *Urocortin3-Cre<sup>47</sup>* and *Rosa26-Lox-Stop-Lox-H2BmCherry<sup>48</sup>* mice were  
301 previously described. All mouse strains were maintained on a mixed genetic background.  
302 Control colony mates in all analyses were *Robo<sup>+/+</sup>* with the either *Ins1-Cre* or *Ucn3-Cre*.

303

### 304 **Immunofluorescence**

305 Pancreata were fixed with 4% PFA at 4°C for 3h, embedded in 30% sucrose and frozen in OCT  
306 (Tissue-Tek). Pancreatic sections (10 μm) were stained using a standard protocol. The following  
307 primary antibodies and dilutions were used: guinea pig anti-Insulin (1:6, Dako, IR00261-2),  
308 mouse anti-Glucagon (1:500, Sigma G2654), rabbit anti-Glucagon (1:200, Cell Signaling 2760S),  
309 rabbit anti-Somatostatin (1:1000, Phoenix G-060-03), rabbit anti-Connexin36 (1:80, Invitrogen  
310 36-4600), rabbit anti-Col IV (1:300, Abcam Ab656), rat anti-Laminin β1 (1:500, Invitrogen MA5-  
311 14657). The following secondary antibodies were used at 1:500: Donkey anti-Guinea Pig 594  
312 (Jackson), Donkey anti-Guinea Pig 647 (Jackson), Donkey anti-Rabbit 488 (Invitrogen), Donkey  
313 anti-Rabbit 594 (Invitrogen), Donkey anti-goat 647 (Invitrogen), and Donkey anti-rat 488  
314 (Invitrogen). Slides were imaged using a Leica SP8 Scanning Confocal microscope or a Zeiss Axio  
315 Observer.Z1 microscope.

316

317 **RNA sequencing**

318 RNA was isolated from FACS sorted lineage-traced  $\beta$  cells<sup>36</sup> from control and *Robo*  $\beta$ KO mice  
319 using phenol chloroform extraction (TRIzol). DNA libraries were generated using Takara's  
320 SMART-Seq v4 Low Input RNA Kit for Sequencing (Takara, Mountain View, California, USA) for  
321 cDNA synthesis and the Illumina NexteraXT DNA Library Preparation (Illumina, San Diego, CA,  
322 USA) kit for cDNA dual indexing. Full length cDNA fragments were generated from 1-10ng total  
323 RNA by SMART (Switching Mechanism at 5' End of RNA Template) technology. cDNA fragments  
324 were fragmented and dual indexed in a single step using the Nextera kit's simultaneous  
325 transposon and tagmentation step. Quality and quantity of completed libraries were assessed  
326 using Agilent DNA series chip assay (Agilent Technologies, Santa Clara, CA) and Invitrogen Qubit  
327 ds DNA HS Kit (Invitrogen, Carlsbad, California, USA), respectively. Each library was standardized  
328 to 2nM. Cluster generation was performed on Illumina cBot, with libraries multiplexed for  
329 1x100bp sequencing using TruSeq 100bp SBS kit (v4) on an Illumina HiSeq2500. Images were  
330 analyzed using standard Illumina Pipeline, version 1.8.2.

331

332 **Intravital imaging**

333 Mouse pancreata were exposed in anesthetized mice by making a small incision on the right  
334 side of the mouse, and externalizing the tip of the pancreas. A glass dish was placed over the  
335 exposed pancreas and the mouse was placed on a microscope stage with isoflurane anesthesia  
336 for the remainder of imaging. Islets were identified on the surface of the pancreas by detecting  
337 Histone H2B-mCherry fluorescent nuclei labeled by  $\beta$  cell-specific lineage-tracing reporter<sup>36</sup>.

338 Once islets were identified, mice were given injections of 1g/kg body weight glucose (30% in  
339 saline) intraperitoneally. Blood glucose levels were monitored through tail vein bleeds. Once  
340 the blood glucose reached ~300 mg/dL, GCaMP6s activity was identified using the microscope  
341 eye piece. When imaging a time course of GCaMP6s intensity, a z-stack was set to 3, 8 or 12  
342 slices each 8 $\mu$ m apart. Images were captured at 0.2Hz, 0.1Hz, or 0.03Hz respectively over at  
343 least 10 minutes at a resolution of 512x512 pixels. After time courses were recorded, high  
344 resolution image z-stacks were taken with 60 z planes taken 1 $\mu$ m apart or 8 z-planes taken 8 $\mu$ m  
345 apart at 1024x1024 pixel resolution. For some images, rhodamine-dextran was injected retro-  
346 orbitally to mark the vasculature of the islets *in vivo*.

347

#### 348 **Gap junction and vasculature quantification**

349 Cx36 levels were quantified from images of islets co-stained with rabbit anti-Cx36 (Invitrogen)  
350 and Guinea Pig anti-insulin (Dako) antibody. Vasculature levels were quantified from images co-  
351 stained with rat anti-Laminin  $\beta$ 1 (Invitrogen) or rabbit anti-col IV and Guinea Pig anti-insulin  
352 (Dako). 8 Z-planes were taken 1 $\mu$ m apart on a Leica SP8 Scanning Confocal microscope using a  
353 40x oil immersion objective (Cx36) or 20X (vasculature). Threshold masks were made of both  
354 channels for each islets, and the area of each staining was measured using FIJI's analyze  
355 particles functions. The area of gap junctions or blood vessels (marked by their respective  
356 antibody) was divided by the area of DAPI or insulin respectively for each islet. 10-14 islets were  
357 analyzed for  $n=3-8$  mice for each genotype. Student's T-test was performed to obtain  $P$  values.

358

#### 359 **Nearest neighbor analysis**

360  $\beta$  cells were identified using the lineage tracer *Rosa26-Lox-Stop-Lox-H2BmCherry* crossed to  
361 *Ucn3-Cre* and tissue sections were stained with antibodies against glucagon and somatostatin  
362 to identify  $\alpha$  and  $\delta$  cells respectively. The 3D Tissue Spatial Analysis Toolbox for Fiji<sup>49</sup> was used  
363 to identify specific cell types using the above markers and to calculate the number of cell type  
364 specific nearest neighbors from all identified endocrine cells. Analysis was performed on 9-11  
365 islets from  $n=3$  mice from each genotype.

366

### 367 **Time course image analysis**

368 All images were analyzed using previously published methods<sup>50</sup> with custom Matlab  
369 (Mathworks) scripts. For activity analysis, images were smoothed using a 5x5 pixel averaging  
370 filter. Areas without significant fluorescence were removed. Saturated areas were also removed  
371 by limiting the area to intensity below the maximum value. Photobleaching was adjusted for by  
372 removing any linear trend. Any islets with significant motion artifacts were removed or time  
373 courses were shortened to the time over which no significant movement occurred  
374 (displacement of  $<0.5$  cell width). For the time course of each pixel in the image with significant  
375 fluorescence, a peak detection algorithm was used to determine if the areas had peak  
376 amplitudes significantly above background. A region was considered “active” if the  
377 corresponding time course for each pixel had a peak amplitude  $>2.4x$  background. The fraction  
378 of active area was calculated as the number of pixels detected as “active” across all z-planes,  
379 normalized to the total number of pixels that showed significant fluorescence across all z-  
380 planes that were not saturated. Islets with significant background fluorescence from spectral  
381 overlap of channels were excluded from activity analysis because “inactive” cells were

382 indistinguishable from background and therefore total islet area could not be accurately  
383 calculated. Coordination was determined based on coincident timing of identified peaks, where  
384 areas were segmented by identified peaks occurring at similar time points. The cross  
385 correlation of the time courses for two 5x5 pixel subregion was taken. If the correlation  
386 coefficient was  $>0.75$ , then the two subregions were considered highly coordinated and merged  
387 into a larger region. The coordinated area was calculated as the number of pixels in the largest  
388 area of coordination across all z-planes normalized to the total number of pixels of the islet that  
389 were determined to be 'active' for all planes. This analysis is based on previous analysis<sup>50</sup>, but  
390 adjusted for 3-dimensional data. All statistical analysis was performed in Prism (Graphpad) or  
391 Matlab. First a F-test was used to determine if variances were equal then a Student's t-test or  
392 Welch t-test (for unequal variance) were utilized for determining whether activity,  
393 coordination, phase lag and speed were significantly different.  $p < 0.05$  was considered  
394 significant.

395

### 396 ***In vitro* single cell Ca<sup>2+</sup> imaging**

397 Islets were isolated according to standard protocol from 3-6 month old *Robo*  $\beta$ KO and control  
398 mice. For islet dispersion, 12mm round No. 1.5 coverslips contained in a 24-well plate were pre-  
399 coated overnight with 50 $\mu$ L 1:15000 PEI (Sigma P3143) overnight. Groups of 100 mouse islets  
400 were dispersed into single cells in 3mL Accutase (Thermo Fisher A1110501) at 37°C for 10 min.  
401 During the incubation, PEI was replaced with 100 $\mu$ L Geltrex (Thermo Fisher A1413302) and  
402 centrifuged at 500g for 5 min at 4°C, followed by removal of excess Geltrex. The cells were  
403 washed once with islet culture medium (RPMI1640 supplemented with 10% FBS (v/v), 100

404 units/mL penicillin, and 100ug/mL streptomycin (Invitrogen)) and resuspended in 1mL medium  
405 before plating 500 $\mu$ L per coverslip. The plate was centrifuged for 5 minutes at 500g and  
406 cultured overnight before imaging. For measurements of cytosolic Ca<sup>2+</sup>, dispersed islet cells  
407 were pre-incubated in 5 $\mu$ M Fura2-AM (Thermofisher F1201) in islet media containing 11.1mM  
408 glucose for 45 min at 37°C, followed by 15 min incubation in islet media containing 2.7mM  
409 glucose. Coverslips were transferred to a RC-48LP imaging chamber (Warner Instruments)  
410 mounted on a Nikon Ti-Eclipse inverted microscope equipped with a 20X/0.75N.A. SuperFluor  
411 objective and PerfectFocus (Nikon Instruments). The chamber was perfused with a standard  
412 external solution containing 135mM NaCl, 4.8mM KCl, 2.5mM CaCl<sub>2</sub>, 1.2mM MgCl<sub>2</sub>, 20mM  
413 HEPES, and glucose as indicated (pH 7.35). The flow rate was set to 0.4mL/min (Fluigent MCFS-  
414 EZ) and temperature was maintained at 33°C using solution and chamber heaters (Warner  
415 Instruments). Excitation was provided by a SOLA SE II 365 (Lumencor) set to 10% output and an  
416 inline neutral density filter (Nikon ND4). Fluorescence emission was collected with a  
417 Hamamatsu ORCA-Flash4.0 V2 Digital CMOS camera at 0.1Hz. Excitation (x) and emission (m)  
418 filters were used in combination with a ET FURA2/GFP C164605 dichroic (Chroma): Fura2,  
419 ET365/20x, ET535/30m; mCherry ET572/35x and ET632/60m.  $\beta$  cells were identified by the  
420 expression of mCherry. Baseline-normalized cytosolic calcium was quantified using Nikon  
421 Elements and GraphPad Prism software.



422 **Figure Legends**

423 **Figure 1: *Robo*  $\beta$ KO islets have a smaller fraction of homotypic nearest neighbors than**  
424 **controls** (A) Immunofluorescence images (left and middle panels) and cell connectivity maps  
425 generated by nearest neighbor analysis (right panels) of control and *Robo*  $\beta$ KO islets.  $\beta$  cells  
426 (red),  $\alpha$  cells (green), and  $\delta$  cells (blue) are denoted by nodes on the connectivity maps. A line  
427 the same color as both nodes it connects denotes a homotypic interaction of that  
428 corresponding cell type. A white line connecting two nodes denotes a heterotypic interaction  
429 between cell types. (B) Probability of  $\beta$  cell- $\beta$  cell contacts in *Robo*  $\beta$ KO islets vs. controls ( $n=9$ -  
430 11 islets for 3 mice from each genotype; control  $75.35\% \pm 4.1$ , *Robo*  $\beta$ KO  $50.37\% \pm 4.1$ ,  $p=0.01$ ). (C)  
431 Probability of any homotypic cell-cell contact in *Robo*  $\beta$ KO islets vs controls ( $n=9$ -11 islets for 3  
432 mice from each genotype; control  $83.7\% \pm 1.7$ , *Robo*  $\beta$ KO  $64.43\% \pm 1.2$ ,  $p=0.0008$ ). (D) Probability  
433 of  $\beta$  cell-  $\alpha$  cell contacts in *Robo*  $\beta$ KO islets vs controls ( $n=9$ -11 islets for 3 mice from each  
434 genotype; control  $11.21\% \pm 2.7$ , *Robo*  $\beta$ KO  $25.99\% \pm 3.0$ ,  $p=0.02$ ). (E) Probability of any  
435 heterotypic cell-cell contact in *Robo*  $\beta$ KO islets vs. controls ( $n=9$ -11 islets for 3 mice from each  
436 genotype; control  $16.3\% \pm 1.7$ , *Robo*  $\beta$ KO  $35.57\% \pm 1.2$ ,  $p=0.0008$ ). (B-E Similar shaded points in  
437 graphs indicate islets from the same mouse).

438

439 **Figure 2: Control islets show highly synchronized whole islet  $\text{Ca}^{2+}$  oscillations** (A) High  
440 resolution maximum intensity projection of a control islet *in vivo* in an *AAV8-RIP-GCaMP6s*-  
441 injected mouse showing GCaMP6s in green, nuclear mCherry  $\beta$  cell lineage-tracing in red, and  
442 collagen (second-harmonic fluorescence) in blue. (B) Stills over one oscillation period from  
443 control islet in supplementary video 1, starting after blood glucose level reached  $\sim 300\text{mg/dL}$

444 from IP glucose injection. Video was recorded for 10 minutes with an acquisition speed of  
445 0.1Hz. (C) Representative time courses of  $\text{Ca}^{2+}$  activity in 4 individual areas from control islet in  
446 supplementary video 1 showing correlation over 98% of the active islet area. Time courses are  
447 normalized to average fluorescence of individual area over time. Similar color indicates that the  
448 time courses have a Pearson's correlation coefficient of  $\geq 0.75$  and matches the region of  
449 coordination that is seen in D. (D) False color map of top five largest coordinated areas across z-  
450 stack of control islet from analysis in C. Areas in grey are not coordinated. The color represents  
451 a region of coordination with Pearson's Correlation Coefficient  $\geq 0.75$  of GCaMP6s activity. Cells  
452 used in time courses in C are labeled.

453

454 **Figure 3: *Robo*  $\beta$ KO islets show uncoordinated whole islet  $\text{Ca}^{2+}$  oscillations** (A) High resolution  
455 maximum intensity projection of a *Robo*  $\beta$ KO islet *in vivo* in an AAV8-RIP-GCaMP6s-injected  
456 mouse showing GCaMP6s in green, nuclear mCherry  $\beta$  cell lineage-tracing in red, and collagen  
457 (second-harmonic fluorescence) in blue. (B) Stills over one oscillation period from *Robo*  $\beta$ KO  
458 islet in supplemental video 4, starting after blood glucose level reached  $\sim 300$ mg/dL from IP  
459 glucose injection. Video was recorded for 10 minutes with an acquisition speed of 0.1Hz. (C)  
460 Representative time courses of  $\text{Ca}^{2+}$  activity in 4 individual areas from *Robo*  $\beta$ KO islet in  
461 supplementary video 4, showing correlation of 50% of the active islet area. Time courses are  
462 normalized to average fluorescence of individual area over time. Similar color indicates that the  
463 time courses. Similar color indicates that the time courses have a Pearson's correlation  
464 coefficient of  $\geq 0.75$  and matches the region of coordination that is seen in D. (D) False color  
465 map of top five largest coordinated areas across z-stack of *Robo*  $\beta$ KO islet from analysis in C.

466 Areas in grey are not coordinated. The color represents a region of coordination with Pearson's  
467 correlation coefficient of  $\geq 0.75$  of GCaMP6s activity.

468

469 **Figure 4: Quantification of *Robo*  $\beta$ KO  $Ca^{2+}$  oscillation phenotype** (A) Largest fraction of area in  
470 islet exhibiting coordinated  $Ca^{2+}$  oscillations for control and *Robo*  $\beta$ KO islets. (B) Fraction of  
471 active islet area showing elevated  $Ca^{2+}$  activity for control and *Robo*  $\beta$ KO islets.

472

473 **Figure 5: Dissociated *Robo*  $\beta$ KO  $\beta$  cells show no difference in glucose stimulated  $Ca^{2+}$**   
474 **oscillations** (A) Representative  $Ca^{2+}$  trace (Fura2) of a single dispersed  $\beta$  cell from a control islet.  
475 10G line marks the addition of 10mM glucose. (B) Representative  $Ca^{2+}$  trace (Fura2) of a  
476 dispersed  $\beta$  cell from a *Robo*  $\beta$ KO islet. 10G line marks the addition of 10mM glucose. (C) Graph  
477 showing the proportion of  $Ca^{2+}$  responsive  $\beta$  cells in *Robo*  $\beta$ KO compared to controls (D) Graph  
478 showing peak height of  $Ca^{2+}$  oscillation corresponding to first phase insulin secretion from  
479 control and *Robo*  $\beta$ KO single dispersed  $\beta$  cells in response to 10mM glucose. (E) Graph showing  
480 area under the curve (AUC) of  $Ca^{2+}$  oscillations (Fura2) from control and *Robo*  $\beta$ KO single  
481 dispersed  $\beta$  cells in response to 10mM glucose. (F) Graph showing area under the curve (AUC)  
482 of  $Ca^{2+}$  oscillations (Fura2) from control and *Robo*  $\beta$ KO single dispersed  $\beta$  cells in response to  
483 KCL.

484

485 **Figure 6: Amount of Cx36 gap junctions remains unchanged in *Robo*  $\beta$ KO** (A)  
486 Immunofluorescent images showing Cx36 (gray or green) and insulin (red) in Control, *Robo*  
487 *\beta*KO, and *Cx36* KO islets. (B) Quantification of area of Cx36 staining normalized to islet area in

488 *Robo*  $\beta$ KO islets and controls showing no significant difference ( $n=10-20$  islets from 2-4 mice per  
489 group,  $p$  values shown). similar colored dots represent islet from the same mouse (C)  
490 Immunofluorescent images showing histone H2B-mCherry  $\beta$  cell lineage trace in red, F-Actin  
491 (phalloidin) in blue, and Cx36 in yellow demonstrating normal localization of Cx36 to plasma  
492 membrane (visible as white dots) of  $\beta$  cells in both control and *Robo*  $\beta$ KO islets.

493

494 **Figure 7: Amount of vascularization remains unchanged in *Robo*  $\beta$ KO islets** (A) Representative  
495 immunofluorescent staining of Collagen IV marking vasculature showing similar amounts in  
496 *Robo*  $\beta$ KO and control islets (B) Quantification of area of Collagen IV staining normalized to islet  
497 area showing no difference in amounts of basement membrane marking blood vessels in *Robo*  
498  $\beta$ KO compared to control islets. (C) Representative immunofluorescent staining of laminin  
499 marking vasculature showing similar amounts in *Robo*  $\beta$ KO and control islets (D) Quantification  
500 of area of laminin staining normalized to islet area showing no difference in amounts of  
501 basement membrane marking blood vessels in *Robo*  $\beta$ KO compared to control islets.

502 **Supplemental Figures**

503 **Supplemental Video 1: Control islets show highly synchronized Ca<sup>2+</sup> oscillations.** Intravital time  
504 course video of an islet within the *in vivo* pancreas of a control  $\beta$  cell lineage traced mouse  
505 infected with *AAV8-Ins1-GCaMP6s*. Lineage traced  $\beta$  cells are marked by mCherry in red and  
506 GCaMP6s is shown in green. Mouse was injected IP with glucose, and video was recorded once  
507 blood glucose levels reached  $\sim$ 300mg/dL. Z-stack of 8 slices each 8 $\mu$ m apart were recorded at  
508 0.1Hz over 10 minutes. Scale bar is 100 $\mu$ m. Time stamp shown in in upper left corner shows  
509 time of image in min:sec.

510

511 **Supplemental Video 2: Control islets show highly synchronized Ca<sup>2+</sup> oscillations.** Intravital time  
512 course video of an islet within the *in vivo* pancreas of a control  $\beta$  cell lineage traced mouse  
513 infected with *AAV8-Ins1-GCaMP6s*. Lineage traced  $\beta$  cells are marked by mCherry in red and  
514 GCaMP6s is shown in green. Mouse was injected IP with glucose, and video was recorded once  
515 blood glucose levels reached  $\sim$ 300mg/dL. Z-stack of 3 slices each 8 $\mu$ m apart were recorded at  
516 0.2Hz over 12 minutes. Scale bar is 100 $\mu$ m. Time stamp shown in in upper left corner shows  
517 time of image in min:sec.

518

519 **Supplemental Video 3: *Robo*  $\beta$ KO islets show unsynchronized Ca<sup>2+</sup> oscillations.** Intravital time  
520 course video of an islet within the *in vivo* pancreas of a *Robo*  $\beta$ KO  $\beta$  cell lineage traced mouse  
521 infected with *AAV8-Ins1-GCaMP6s*, and retro-orbitally injected with rhodamine-dextran to  
522 mark vasculature. Lineage traced  $\beta$  cells are marked by mCherry in red and GCaMP6s is shown  
523 in green, and vasculature is shown in yellow. Mouse was injected IP with glucose, and video

524 was recorded once blood glucose levels reached ~300mg/dL. Z-stack of 12 slices each 8µm  
525 apart were recorded at 0.03Hz over 10 minutes. Scale bar is 100µm. Time stamp shown in in  
526 upper left corner shows time of image in min:sec.

527

528 **Supplemental Video 4: *Robo*  $\beta$ KO islets show unsynchronized  $Ca^{2+}$  oscillations.** Intravital time  
529 course video of an islet within the *in vivo* pancreas of a *Robo*  $\beta$ KO  $\beta$  cell lineage traced mouse  
530 infected with *AAV8-Ins1-GCaMP6s*. Lineage traced  $\beta$  cells are marked by mCherry in red and  
531 GCaMP6s is shown in green. Mouse was injected IP with glucose, and video was recorded once  
532 blood glucose levels reached ~300mg/dL. Z-stack of 8 slices each 8µm apart were recorded at  
533 0.1Hz over 10 minutes. Scale bar is 100µm. Time stamp shown in upper left corner shows time  
534 of image in min:sec.

535

536 **Supplemental Video 5: *Robo*  $\beta$ KO islets show unsynchronized  $Ca^{2+}$  oscillations.** Intravital time  
537 course video of an islet within the *in vivo* pancreas of a *Robo*  $\beta$ KO  $\beta$  cell lineage traced mouse  
538 infected with *AAV8-Ins1-GCaMP6s*. Lineage traced  $\beta$  cells are marked by mCherry in red and  
539 GCaMP6s is shown in green. Mouse was injected IP with glucose, and video was recorded once  
540 blood glucose levels reached ~300mg/dL. Z-stack of 3 slices each 8µm apart were recorded at  
541 0.2Hz over 10 minutes. Scale bar is 100µm. Time stamp shown in upper left corner shows time  
542 of image in min:sec.

543

544 **Supplemental Video 6: A subset of *Robo*  $\beta$ KO islets retain synchronized  $Ca^{2+}$  oscillations.**  
545 Intravital time course video of an islet within the *in vivo* pancreas of a *Robo*  $\beta$ KO  $\beta$  cell lineage

546 traced mouse infected with AAV8-Ins1-GCaMP6s. Lineage traced  $\beta$  cells are marked by mCherry  
547 in red and GCaMP6s is shown in green. Mouse was injected IP with glucose, and video was  
548 recorded once blood glucose levels reached  $\sim$ 300mg/dL. Z-stack of 8 slices each  $8\mu\text{m}$  apart  
549 were recorded at 0.1Hz over 10 minutes. Scale bar is  $100\mu\text{m}$ . Time stamp shown in in upper left  
550 corner shows time of image in min:sec.

551

552 **Supplemental Figure 1: *Robo*  $\beta$ KO islets retain  $\beta$  cell differentiation and maturity markers**

553 Volcano plot of differential gene expression from bulk RNA sequencing on lineage traced FACS  
554 sorted  $\beta$  cells from *Robo*  $\beta$ KO and control mice showing no significant differential gene  
555 expression of markers ( $n=2$  mice from each group) Red lines denote a fold change of 1.5 and  
556 blue line denotes a p value of 0.05.

557

558 **Supplemental Figure 2: *Robo*  $\beta$ KO islets show uncoordinated whole islet  $\text{Ca}^{2+}$  oscillations (A)**

559 High resolution maximum intensity projection of a *Robo*  $\beta$ KO islet *in vivo* in an AAV8-RIP-  
560 GCaMP6s-injected mouse showing GCaMP6s in green, nuclear mCherry  $\beta$  cell lineage tracing in  
561 red, and collagen in blue. (B) Stills over one oscillation period from *Robo*  $\beta$ KO islet in  
562 supplementary video 3, starting after blood glucose level reached  $\sim$ 300mg/dL from IP glucose  
563 injection. Video was recorded for 10 minutes with an acquisition speed of 0.03Hz. (C)  
564 Representative time courses of  $\text{Ca}^{2+}$  activity in 4 individual areas from *Robo*  $\beta$ KO islet in  
565 supplementary video 3, showing correlation of 43.6% of the active islet area. Time courses are  
566 normalized to average fluorescence of individual area over time. Similar color indicates that the  
567 time courses have a Pearson's correlation coefficient of  $\geq 0.75$  and matches the region of

568 coordination that is seen in D. (D) False color map of top five largest coordinated areas across z-  
569 stack of *Robo*  $\beta$ KO islet from analysis in C. Areas in grey are not coordinated. The color  
570 represents a region of coordination with Pearson's Correlation Coefficient  $\geq 0.75$  of GCaMP6s  
571 activity. Cells used in time courses in C are labeled.

572

573 **Supplemental Figure 3: A subset of *Robo*  $\beta$ KO islets show coordinated whole islet  $\text{Ca}^{2+}$**   
574 **oscillations** (A) High resolution maximum intensity projection of a *Robo*  $\beta$ KO islet *in vivo* in an  
575 *AAV8-RIP-GCaMP6s*-injected mouse showing GCaMP6s in green, nuclear mCherry  $\beta$  cell lineage  
576 tracing in red, and collagen in blue. (B) Stills over one oscillation period from *Robo*  $\beta$ KO islet in  
577 supplementary video 6, starting after blood glucose level reached  $\sim 300\text{mg/dL}$  from IP glucose  
578 injection. Video was recorded for 10 minutes with an acquisition speed of 0.1Hz. (C)  
579 Representative time courses of  $\text{Ca}^{2+}$  activity in 4 individual areas from *Robo*  $\beta$ KO islet in  
580 supplementary video 6, showing correlation of 98% of the active islet area. Time courses are  
581 normalized to average fluorescence of individual area over time. Similar color indicates that the  
582 time courses have a Pearson's correlation coefficient of  $\geq 0.75$  and matches the region of  
583 coordination that is seen in D. (D) False color map of top five largest coordinated areas across z-  
584 stack of *Robo*  $\beta$ KO islet from analysis in C. Areas in grey are not coordinated. The color  
585 represents a region of coordination with Pearson's correlation coefficient of  $\geq 0.75$  of GCaMP6s  
586 activity.



## 587 References

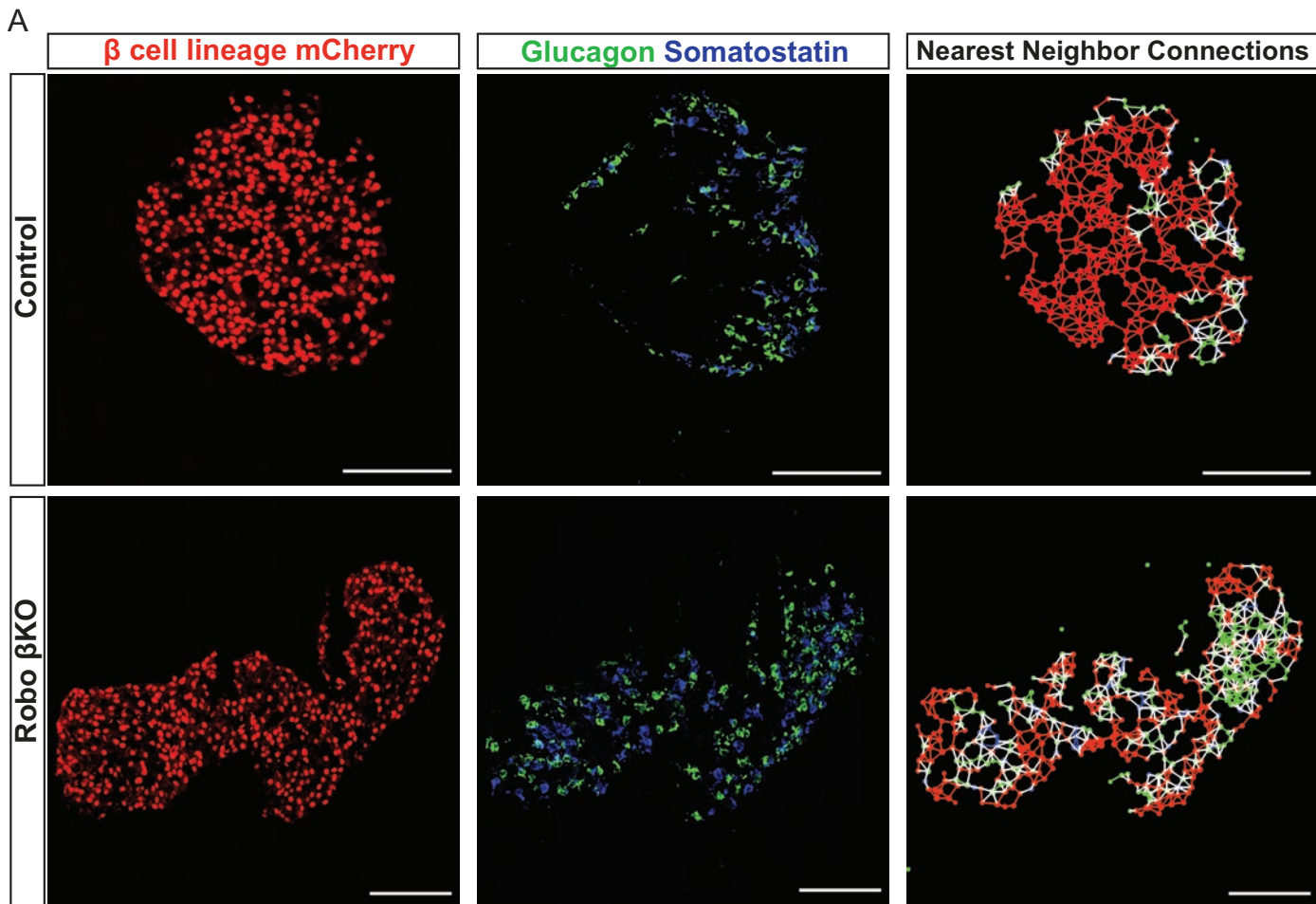
- 588 1 Kim, A. *et al.* Islet architecture: A comparative study. *Islets* **1**, 129-136,  
589 doi:10.4161/isl.1.2.9480 (2009).
- 590 2 Bonner-Weir, S., Sullivan, B. A. & Weir, G. C. Human Islet Morphology Revisited:  
591 Human and Rodent Islets Are Not So Different After All. *The journal of histochemistry*  
592 *and cytochemistry : official journal of the Histochemistry Society* **63**, 604-612,  
593 doi:10.1369/0022155415570969 (2015).
- 594 3 Bosco, D. *et al.* Unique arrangement of alpha- and beta-cells in human islets of  
595 Langerhans. *Diabetes* **59**, 1202-1210, doi:10.2337/db09-1177 (2010).
- 596 4 Brissova, M. *et al.* Assessment of human pancreatic islet architecture and composition by  
597 laser scanning confocal microscopy. *The journal of histochemistry and cytochemistry :  
598 official journal of the Histochemistry Society* **53**, 1087-1097,  
599 doi:10.1369/jhc.5C6684.2005 (2005).
- 600 5 Cabrera, O. *et al.* The unique cytoarchitecture of human pancreatic islets has implications  
601 for islet cell function. *Proceedings of the National Academy of Sciences of the United  
602 States of America* **103**, 2334-2339, doi:10.1073/pnas.0510790103 (2006).
- 603 6 Dybala, M. P. & Hara, M. Heterogeneity of the Human Pancreatic Islet. *Diabetes* **68**,  
604 1230-1239, doi:10.2337/db19-0072 (2019).
- 605 7 Hoang, D. T. *et al.* A conserved rule for pancreatic islet organization. *PloS one* **9**,  
606 e110384, doi:10.1371/journal.pone.0110384 (2014).
- 607 8 Kilimnik, G., Jo, J., Periwal, V., Zielinski, M. C. & Hara, M. Quantification of islet size  
608 and architecture. *Islets* **4**, 167-172, doi:10.4161/isl.19256 (2012).
- 609 9 Hraha, T. H., Bernard, A. B., Nguyen, L. M., Anseth, K. S. & Benninger, R. K.  
610 Dimensionality and size scaling of coordinated Ca(2+) dynamics in MIN6 beta-cell  
611 clusters. *Biophysical journal* **106**, 299-309, doi:10.1016/j.bpj.2013.11.026 (2014).
- 612 10 Nittala, A., Ghosh, S. & Wang, X. Investigating the role of islet cytoarchitecture in its  
613 oscillation using a new beta-cell cluster model. *PloS one* **2**, e983,  
614 doi:10.1371/journal.pone.0000983 (2007).
- 615 11 Ammala, C. *et al.* Exocytosis elicited by action potentials and voltage-clamp calcium  
616 currents in individual mouse pancreatic B-cells. *The Journal of physiology* **472**, 665-688,  
617 doi:10.1113/jphysiol.1993.sp019966 (1993).
- 618 12 Ashcroft, F. M. & Rorsman, P. K(ATP) channels and islet hormone secretion: new  
619 insights and controversies. *Nature reviews. Endocrinology* **9**, 660-669,  
620 doi:10.1038/nrendo.2013.166 (2013).
- 621 13 Bertram, R., Sherman, A. & Satin, L. S. Electrical bursting, calcium oscillations, and  
622 synchronization of pancreatic islets. *Advances in experimental medicine and biology* **654**,  
623 261-279, doi:10.1007/978-90-481-3271-3\_12 (2010).
- 624 14 Bertram, R., Satin, L. S. & Sherman, A. S. Closing in on the Mechanisms of Pulsatile  
625 Insulin Secretion. *Diabetes* **67**, 351-359, doi:10.2337/dbi17-0004 (2018).
- 626 15 Benninger, R. K., Zhang, M., Head, W. S., Satin, L. S. & Piston, D. W. Gap junction  
627 coupling and calcium waves in the pancreatic islet. *Biophysical journal* **95**, 5048-5061,  
628 doi:10.1529/biophysj.108.140863 (2008).
- 629 16 Head, W. S. *et al.* Connexin-36 gap junctions regulate in vivo first- and second-phase  
630 insulin secretion dynamics and glucose tolerance in the conscious mouse. *Diabetes* **61**,  
631 1700-1707, doi:10.2337/db11-1312 (2012).

- 632 17 Brereton, M. F., Vergari, E., Zhang, Q. & Clark, A. Alpha-, Delta- and PP-cells: Are  
633 They the Architectural Cornerstones of Islet Structure and Co-ordination? *The journal of*  
634 *histochemistry and cytochemistry : official journal of the Histochemistry Society* **63**, 575-  
635 591, doi:10.1369/0022155415583535 (2015).
- 636 18 Hang, Y. *et al.* The MafA transcription factor becomes essential to islet beta-cells soon  
637 after birth. *Diabetes* **63**, 1994-2005, doi:10.2337/db13-1001 (2014).
- 638 19 Yamagata, K. *et al.* Overexpression of dominant-negative mutant hepatocyte nuclear  
639 factor-1 alpha in pancreatic beta-cells causes abnormal islet architecture with decreased  
640 expression of E-cadherin, reduced beta-cell proliferation, and diabetes. *Diabetes* **51**, 114-  
641 123 (2002).
- 642 20 Gannon, M. *et al.* Persistent expression of HNF6 in islet endocrine cells causes disrupted  
643 islet architecture and loss of beta cell function. *Development* **127**, 2883-2895 (2000).
- 644 21 Gu, C. *et al.* Pancreatic beta cells require NeuroD to achieve and maintain functional  
645 maturity. *Cell metabolism* **11**, 298-310, doi:10.1016/j.cmet.2010.03.006 (2010).
- 646 22 Ahlgren, U., Jonsson, J., Jonsson, L., Simu, K. & Edlund, H. beta-cell-specific  
647 inactivation of the mouse *Ipf1/Pdx1* gene results in loss of the beta-cell phenotype and  
648 maturity onset diabetes. *Genes & development* **12**, 1763-1768 (1998).
- 649 23 Borden, P., Houtz, J., Leach, S. D. & Kuruvilla, R. Sympathetic innervation during  
650 development is necessary for pancreatic islet architecture and functional maturation. *Cell*  
651 *reports* **4**, 287-301, doi:10.1016/j.celrep.2013.06.019 (2013).
- 652 24 Doyle, M. J. & Sussel, L. *Nkx2.2* regulates beta-cell function in the mature islet.  
653 *Diabetes* **56**, 1999-2007, doi:10.2337/db06-1766 (2007).
- 654 25 Sinagoga, K. L. *et al.* Distinct roles for the mTOR pathway in postnatal morphogenesis,  
655 maturation and function of pancreatic islets. *Development* **144**, 2402-2414,  
656 doi:10.1242/dev.146316 (2017).
- 657 26 Huang, C. *et al.* Synaptotagmin 4 Regulates Pancreatic beta Cell Maturation by  
658 Modulating the Ca(2+) Sensitivity of Insulin Secretion Vesicles. *Developmental cell* **45**,  
659 347-361 e345, doi:10.1016/j.devcel.2018.03.013 (2018).
- 660 27 Jimenez-Caliani, A. J. *et al.* alphaE-Catenin Is a Positive Regulator of Pancreatic Islet  
661 Cell Lineage Differentiation. *Cell reports* **20**, 1295-1306,  
662 doi:10.1016/j.celrep.2017.07.035 (2017).
- 663 28 Bastidas-Ponce, A. *et al.* *Foxa2* and *Pdx1* cooperatively regulate postnatal maturation of  
664 pancreatic beta-cells. *Molecular metabolism* **6**, 524-534,  
665 doi:10.1016/j.molmet.2017.03.007 (2017).
- 666 29 Crawford, L. A. *et al.* Connective tissue growth factor (CTGF) inactivation leads to  
667 defects in islet cell lineage allocation and beta-cell proliferation during embryogenesis.  
668 *Mol Endocrinol* **23**, 324-336, doi:10.1210/me.2008-0045 (2009).
- 669 30 Szabat, M. *et al.* Reduced Insulin Production Relieves Endoplasmic Reticulum Stress and  
670 Induces beta Cell Proliferation. *Cell metabolism* **23**, 179-193,  
671 doi:10.1016/j.cmet.2015.10.016 (2016).
- 672 31 Brissova, M. *et al.* Islet microenvironment, modulated by vascular endothelial growth  
673 factor-A signaling, promotes beta cell regeneration. *Cell metabolism* **19**, 498-511,  
674 doi:10.1016/j.cmet.2014.02.001 (2014).
- 675 32 Baetens, D. *et al.* Alteration of islet cell populations in spontaneously diabetic mice.  
676 *Diabetes* **27**, 1-7 (1978).

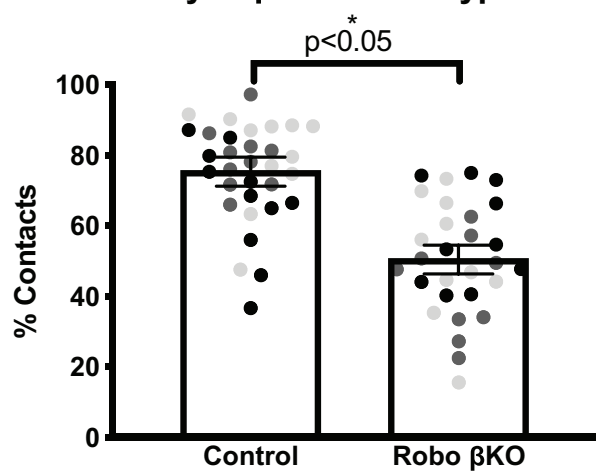
- 677 33 Starich, G. H., Zafirova, M., Jablenska, R., Petkov, P. & Lardinois, C. K. A  
678 morphological and immunohistochemical investigation of endocrine pancreata from  
679 obese ob+/ob+ mice. *Acta histochemica* **90**, 93-101, doi:10.1016/S0065-1281(11)80167-  
680 4 (1991).
- 681 34 Kilimnik, G. *et al.* Altered islet composition and disproportionate loss of large islets in  
682 patients with type 2 diabetes. *PLoS one* **6**, e27445, doi:10.1371/journal.pone.0027445  
683 (2011).
- 684 35 Nir, T., Melton, D. A. & Dor, Y. Recovery from diabetes in mice by beta cell  
685 regeneration. *The Journal of clinical investigation* **117**, 2553-2561,  
686 doi:10.1172/JCI32959 (2007).
- 687 36 Adams, M. T., Gilbert, J. M., Hinojosa Paiz, J., Bowman, F. M. & Blum, B. Endocrine  
688 cell type sorting and mature architecture in the islets of Langerhans require expression of  
689 Roundabout receptors in beta cells. *Scientific reports* **8**, 10876, doi:10.1038/s41598-018-  
690 29118-x (2018).
- 691 37 Hoang, D. T., Hara, M. & Jo, J. Design Principles of Pancreatic Islets: Glucose-  
692 Dependent Coordination of Hormone Pulses. *PLoS one* **11**, e0152446,  
693 doi:10.1371/journal.pone.0152446 (2016).
- 694 38 Reissaus, C. A. *et al.* A Versatile, Portable Intravital Microscopy Platform for Studying  
695 Beta-cell Biology In Vivo. *Scientific reports* **9**, 8449, doi:10.1038/s41598-019-44777-0  
696 (2019).
- 697 39 Yang, Y. H., Manning Fox, J. E., Zhang, K. L., MacDonald, P. E. & Johnson, J. D.  
698 Intra-islet SLIT-ROBO signaling is required for beta-cell survival and potentiates insulin  
699 secretion. *Proceedings of the National Academy of Sciences of the United States of*  
700 *America* **110**, 16480-16485, doi:10.1073/pnas.1214312110 (2013).
- 701 40 Ravier, M. A. *et al.* Loss of connexin36 channels alters beta-cell coupling, islet  
702 synchronization of glucose-induced Ca<sup>2+</sup> and insulin oscillations, and basal insulin  
703 release. *Diabetes* **54**, 1798-1807 (2005).
- 704 41 Blockus, H. & Chedotal, A. Slit-Robo signaling. *Development* **143**, 3037-3044,  
705 doi:10.1242/dev.132829 (2016).
- 706 42 Gan, W. J. *et al.* Cell polarity defines three distinct domains in pancreatic beta-cells.  
707 *Journal of cell science* **130**, 143-151, doi:10.1242/jcs.185116 (2017).
- 708 43 Farnsworth, N. L., Hemmati, A., Pozzoli, M. & Benninger, R. K. Fluorescence recovery  
709 after photobleaching reveals regulation and distribution of connexin36 gap junction  
710 coupling within mouse islets of Langerhans. *The Journal of physiology* **592**, 4431-4446,  
711 doi:10.1113/jphysiol.2014.276733 (2014).
- 712 44 Satin, L. S., Zhang, Q. & Rorsman, P. "Take Me To Your Leader": An  
713 Electrophysiological Appraisal of the Role of Hub Cells in Pancreatic Islets. *Diabetes* **69**,  
714 830-836, doi:10.2337/dbi19-0012 (2020).
- 715 45 Branchfield, K. *et al.* Pulmonary neuroendocrine cells function as airway sensors to  
716 control lung immune response. *Science* **351**, 707-710, doi:10.1126/science.aad7969  
717 (2016).
- 718 46 Thorens, B. *et al.* Ins1(Cre) knock-in mice for beta cell-specific gene recombination.  
719 *Diabetologia* **58**, 558-565, doi:10.1007/s00125-014-3468-5 (2015).
- 720 47 van der Meulen, T. *et al.* Virgin Beta Cells Persist throughout Life at a Neogenic Niche  
721 within Pancreatic Islets. *Cell metabolism* **25**, 911-926 e916,  
722 doi:10.1016/j.cmet.2017.03.017 (2017).

- 723 48 Blum, B. *et al.* Reversal of beta cell de-differentiation by a small molecule inhibitor of  
724 the TGFbeta pathway. *eLife* **3**, e02809, doi:10.7554/eLife.02809 (2014).
- 725 49 Tran Thi Nhu, H., Arrojo, E. D. R., Berggren, P. O. & Boudier, T. A novel toolbox to  
726 investigate tissue spatial organization applied to the study of the islets of Langerhans.  
727 *Scientific reports* **7**, 44261, doi:10.1038/srep44261 (2017).
- 728 50 Westacott, M. J. *et al.* Age-Dependent Decline in the Coordinated [Ca(2+)] and Insulin  
729 Secretory Dynamics in Human Pancreatic Islets. *Diabetes* **66**, 2436-2445,  
730 doi:10.2337/db17-0137 (2017).
- 731
- 732

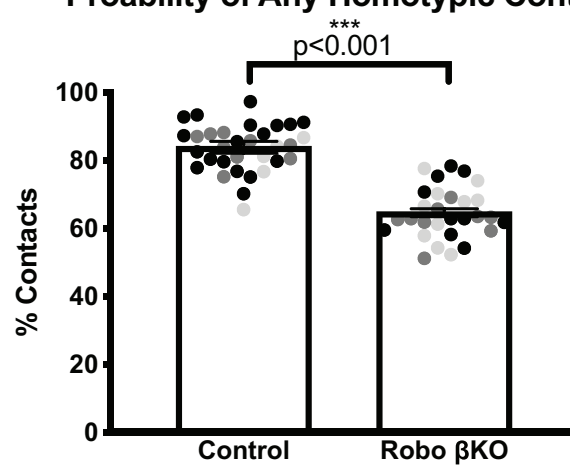
# Figure 1



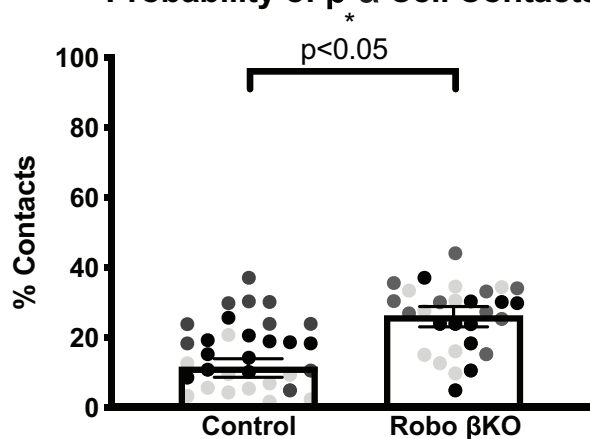
**B** Probability of  $\beta$  Cell Homotypic Contacts



**C** Probability of Any Homotypic Contact



**D** Probability of  $\beta$ - $\alpha$  Cell Contacts



**E** Probability of Any Heterotypic Contact

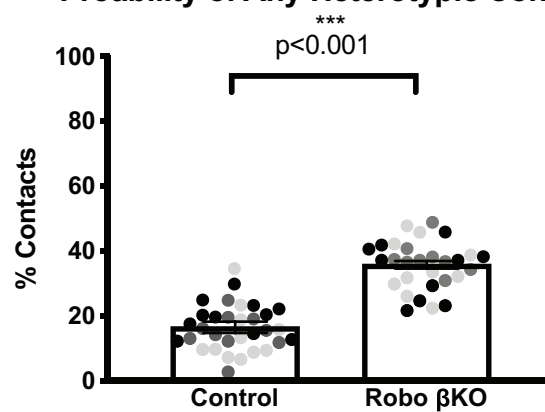




## Figure 2

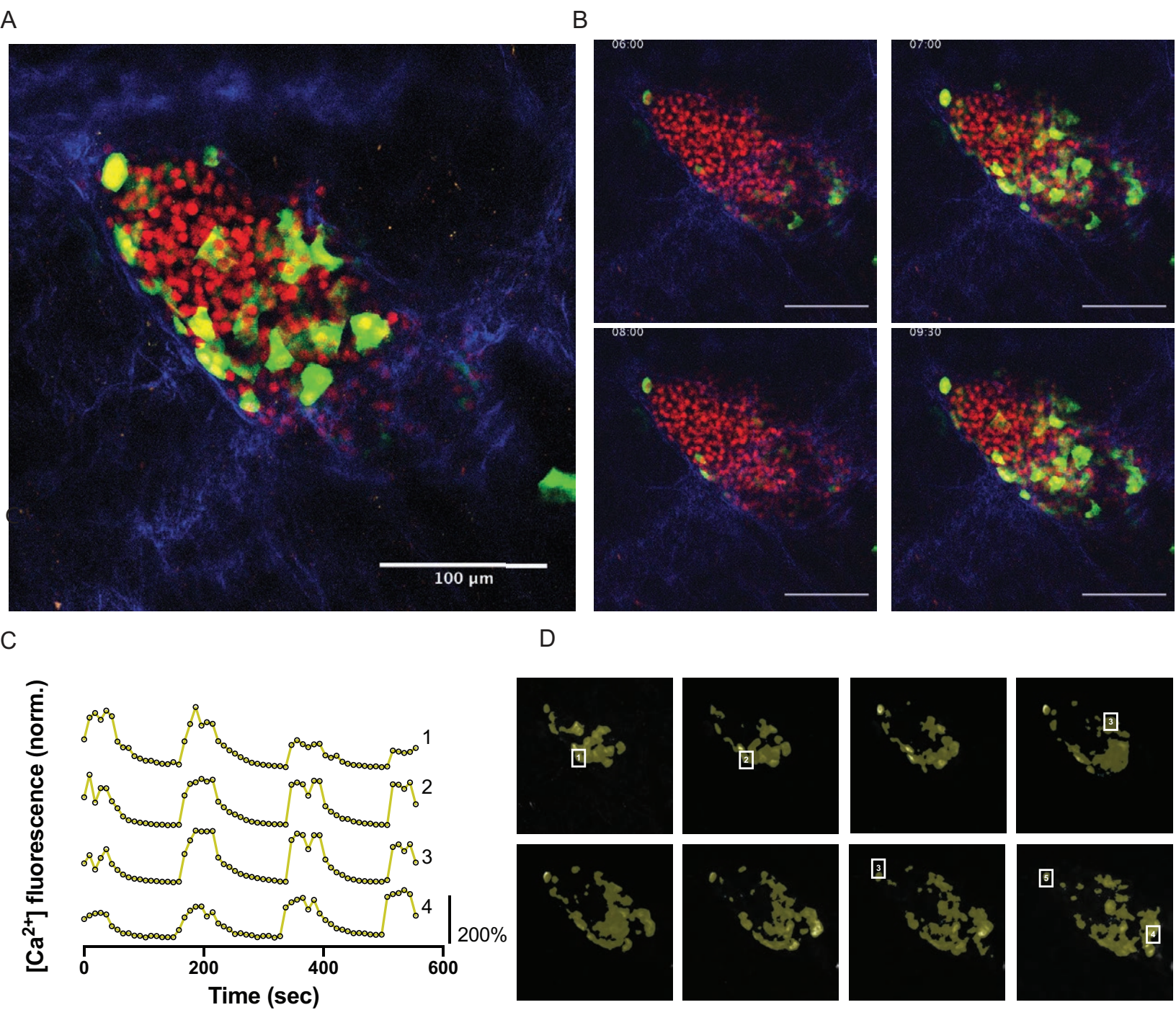
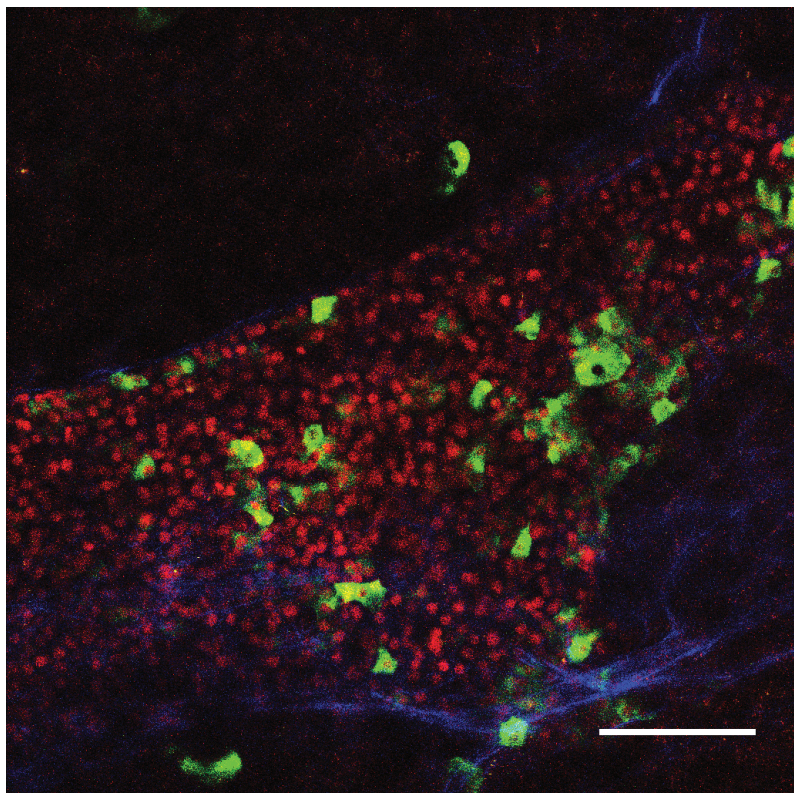


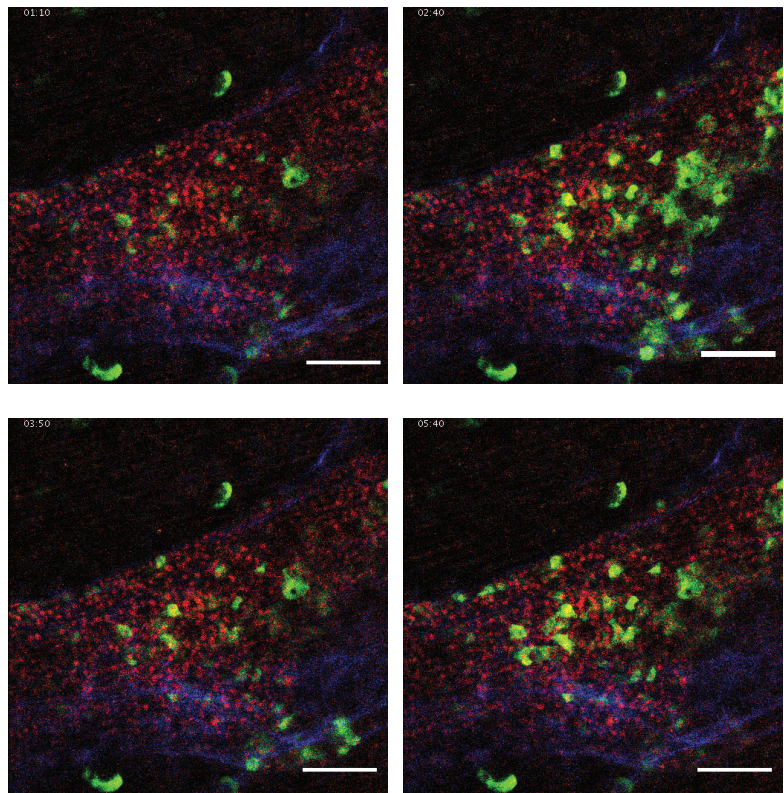


## Figure 3

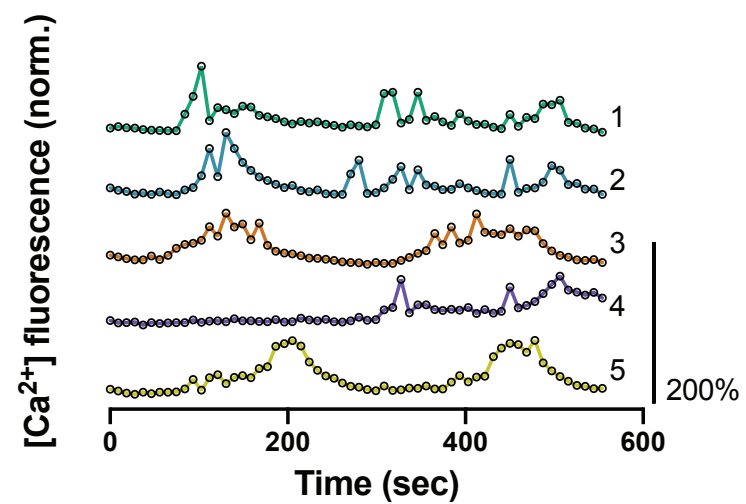
A



B



C



D

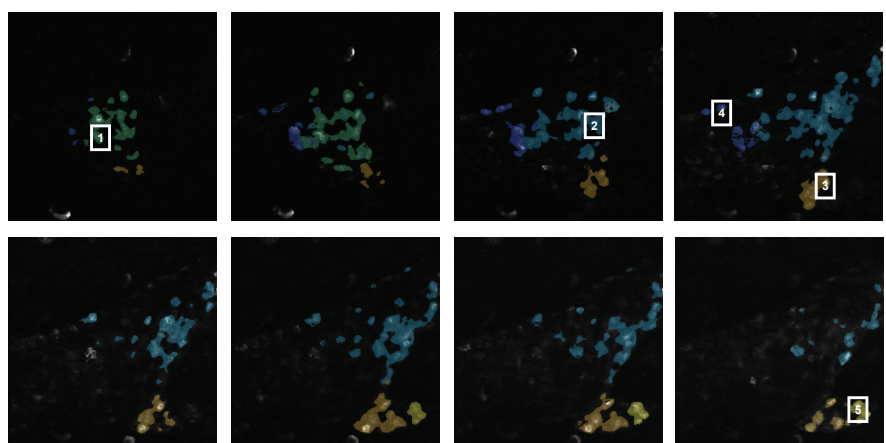


## Figure 4

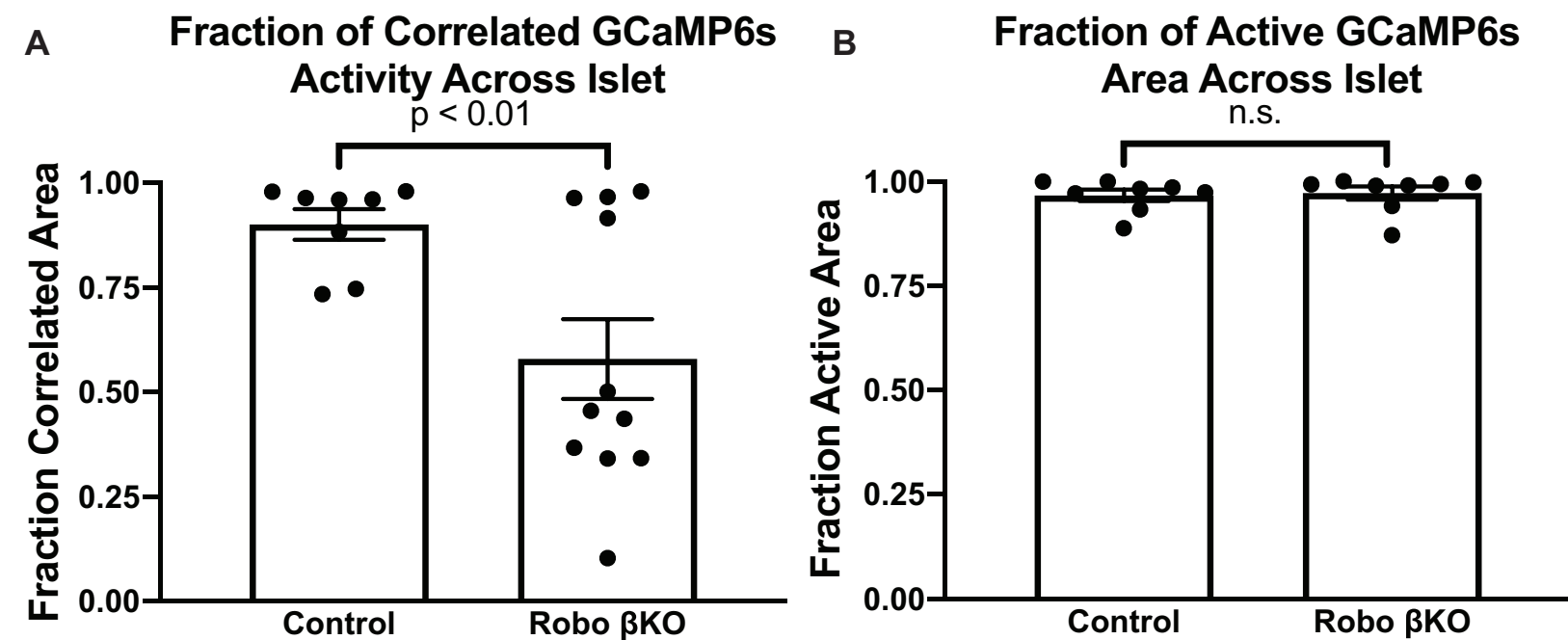




# Figure 5

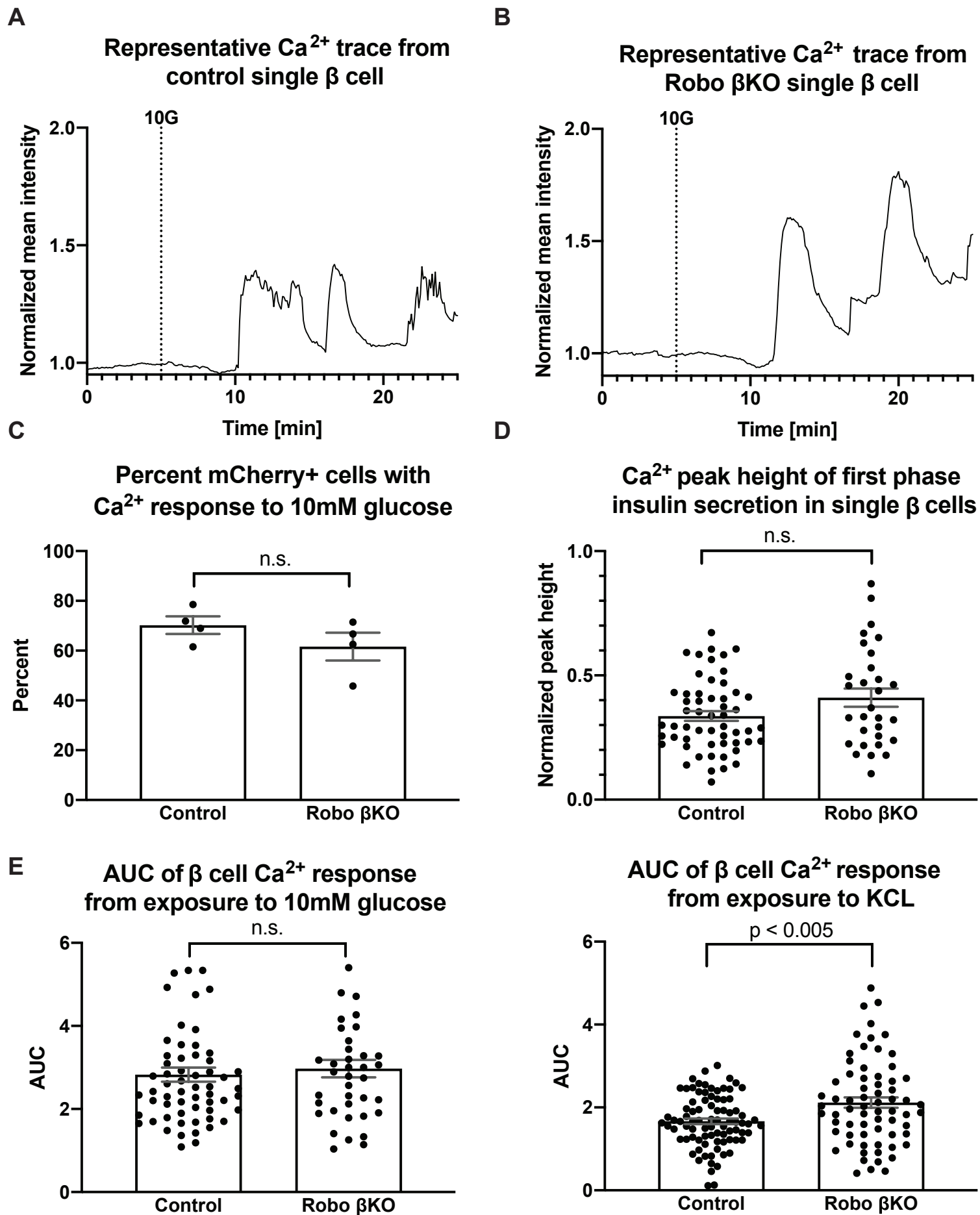


# Figure 6

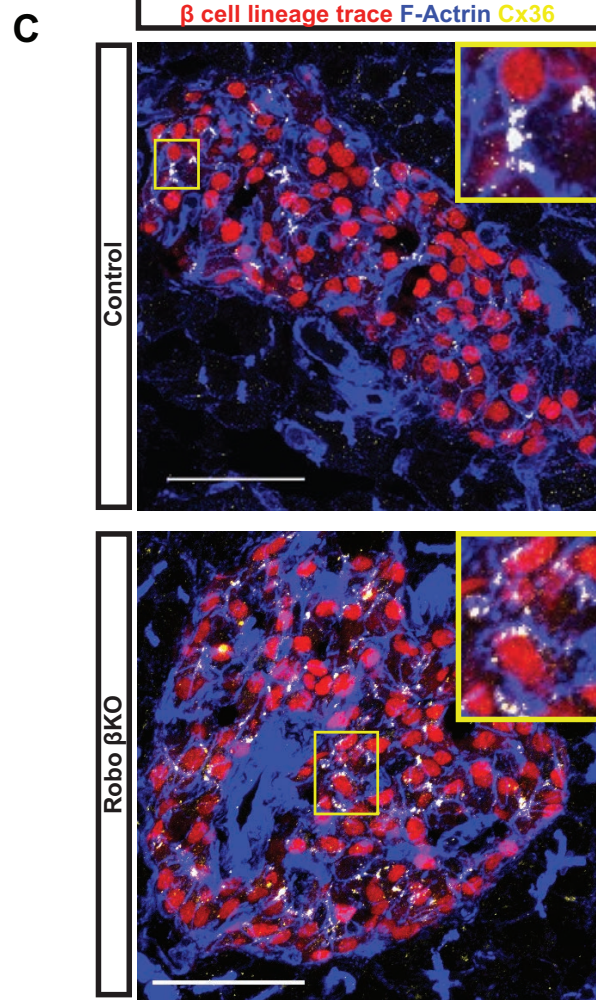
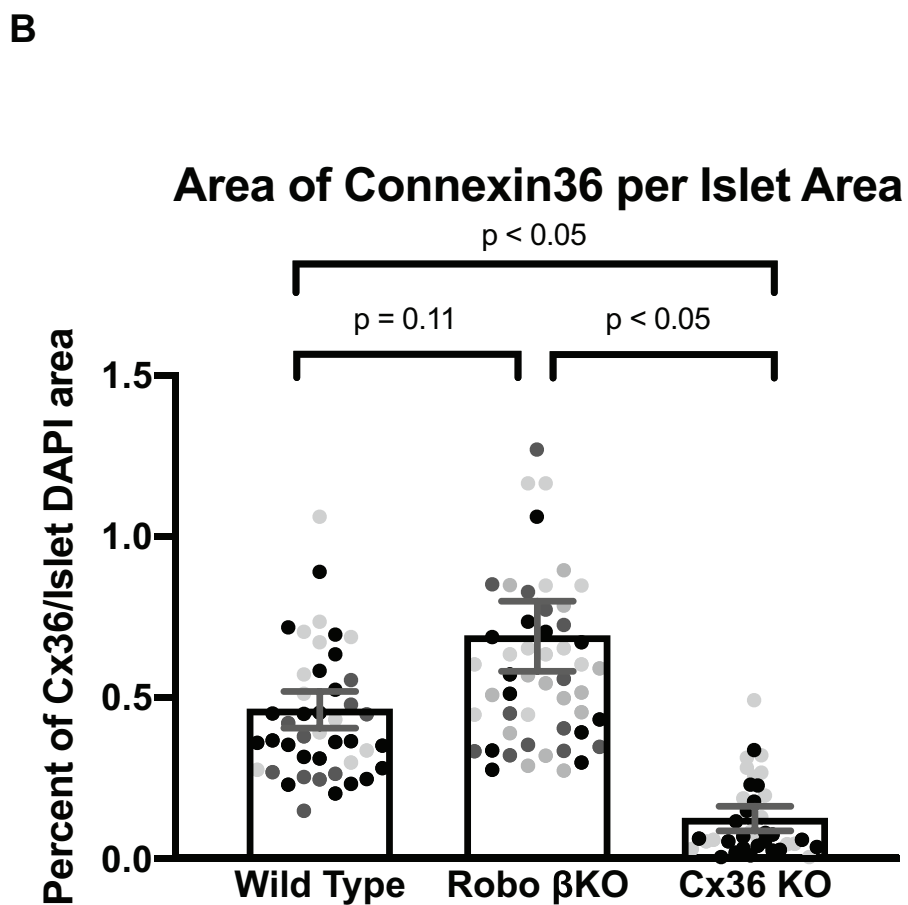
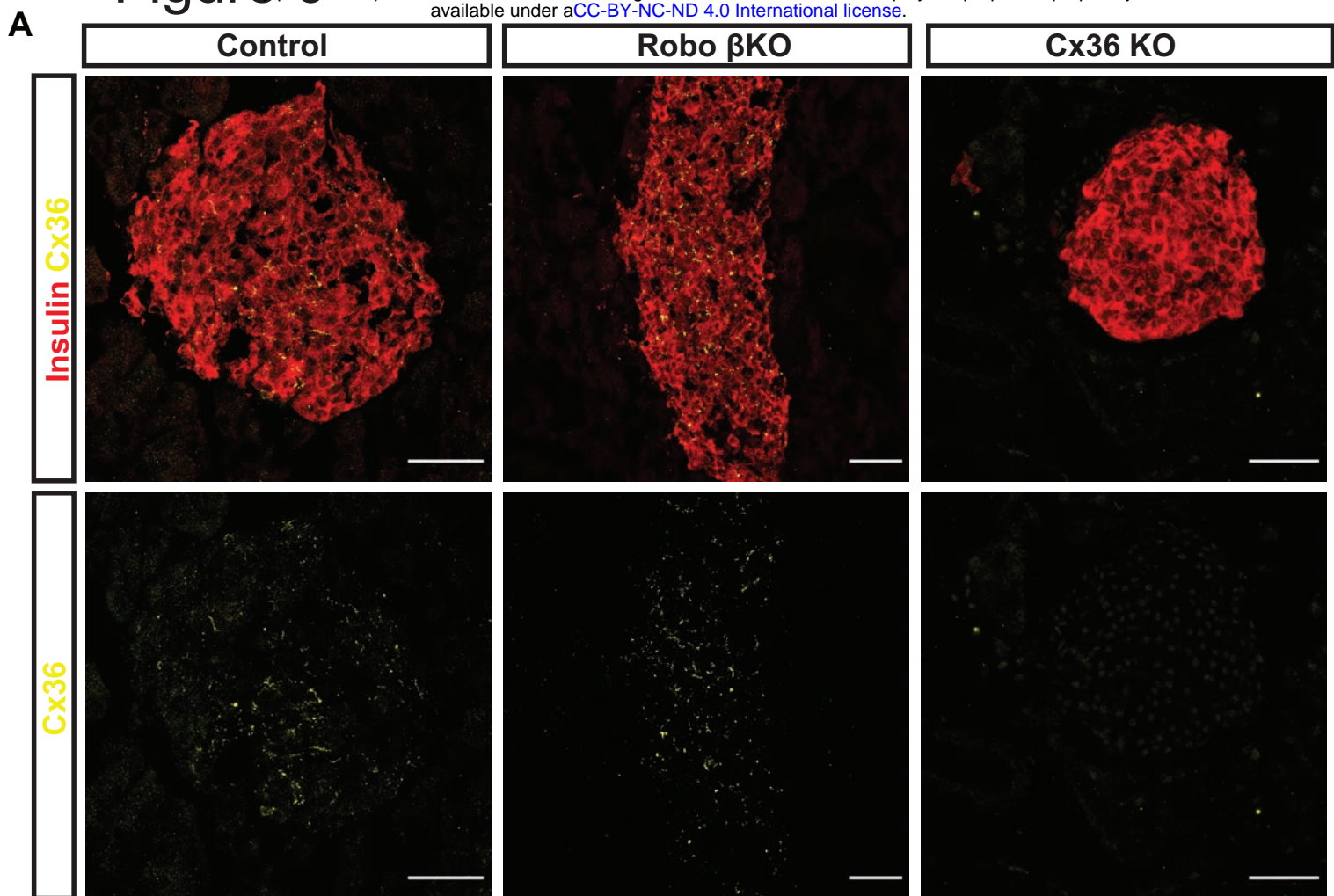
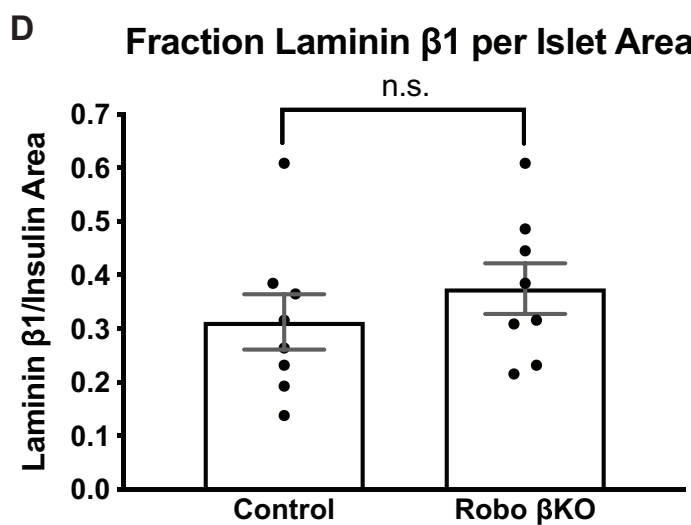
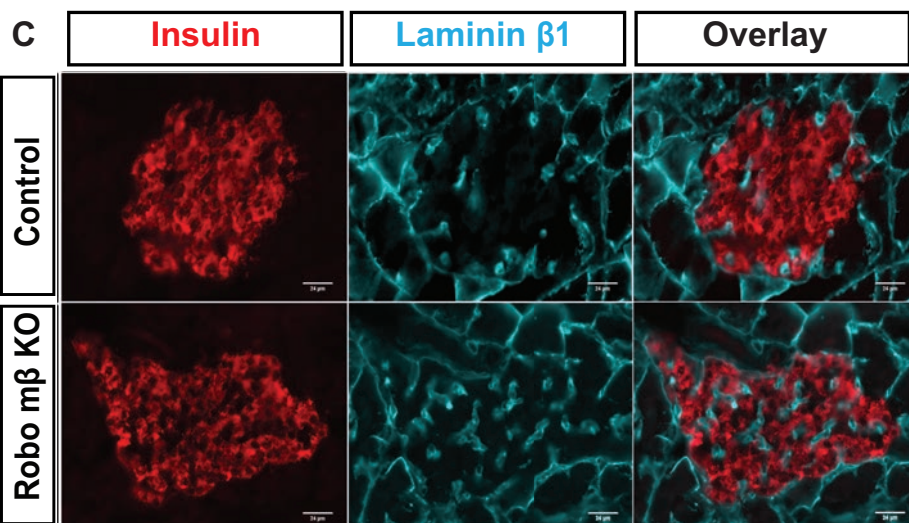
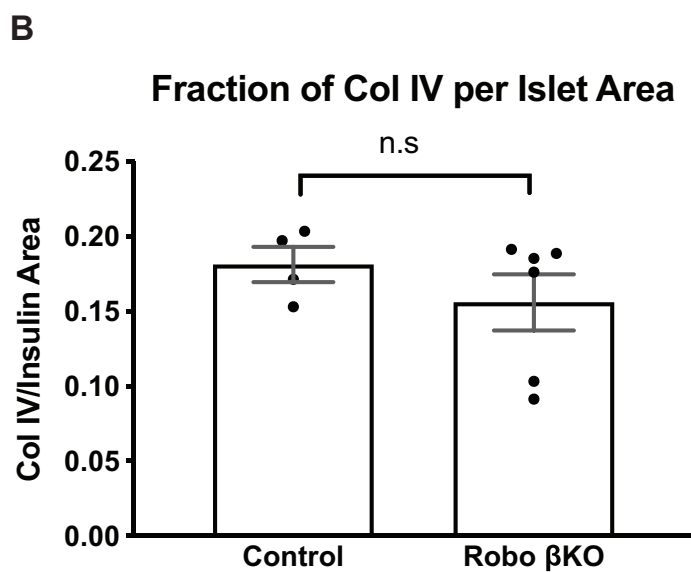
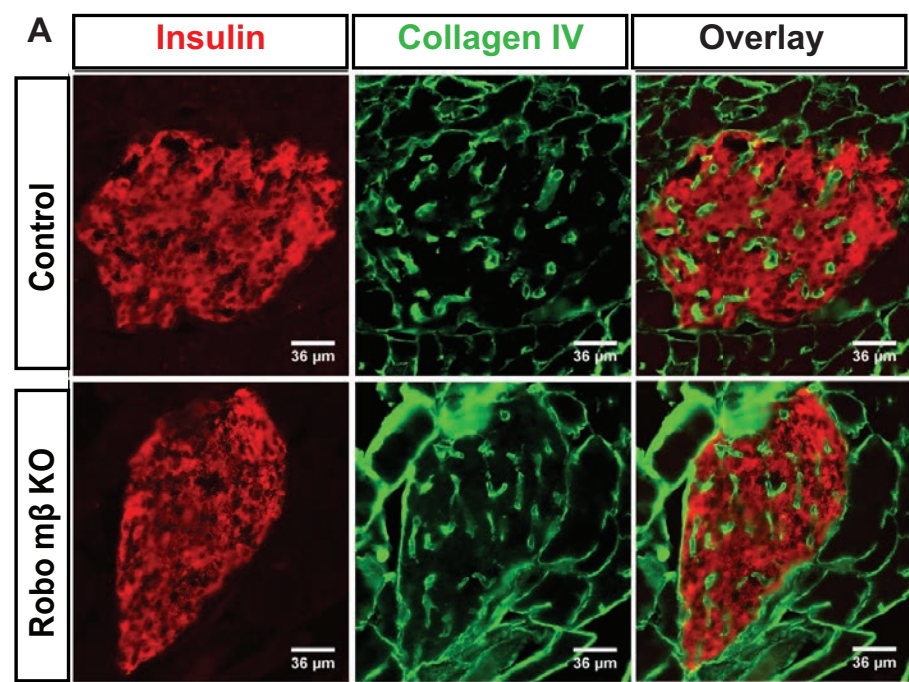
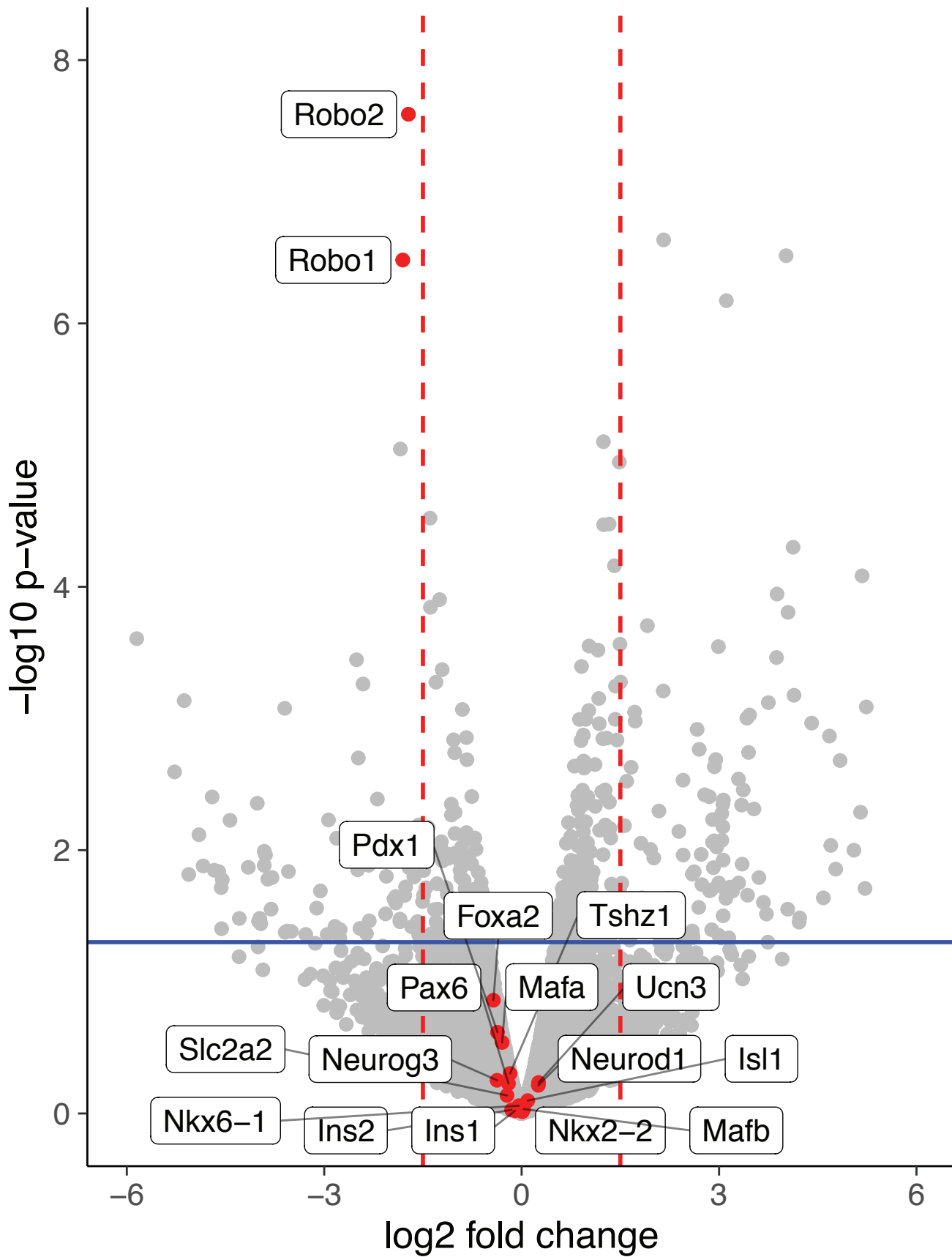


## Figure 7



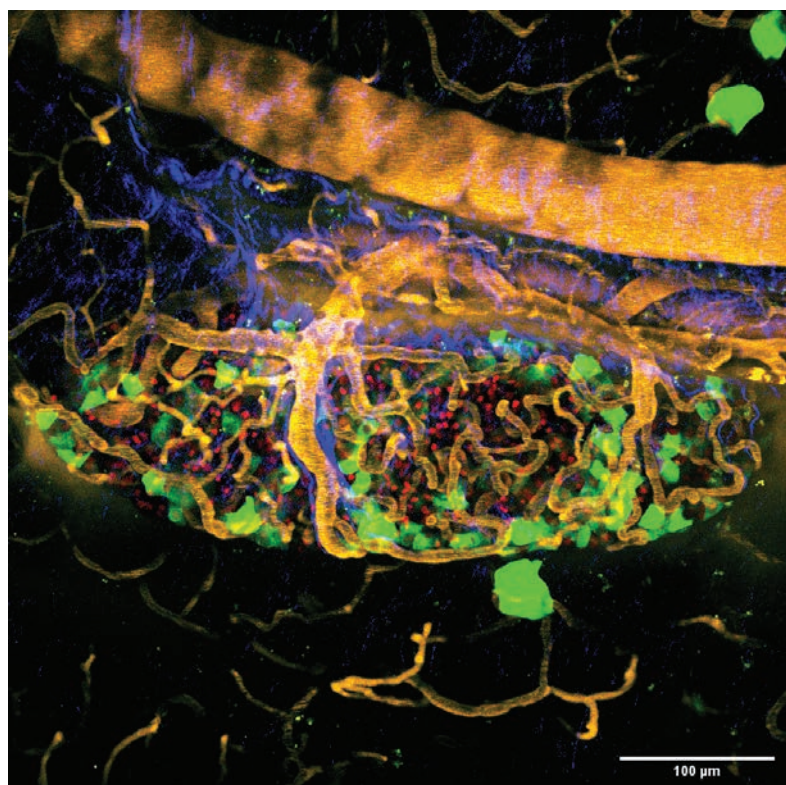


# Supplemental Figure 1

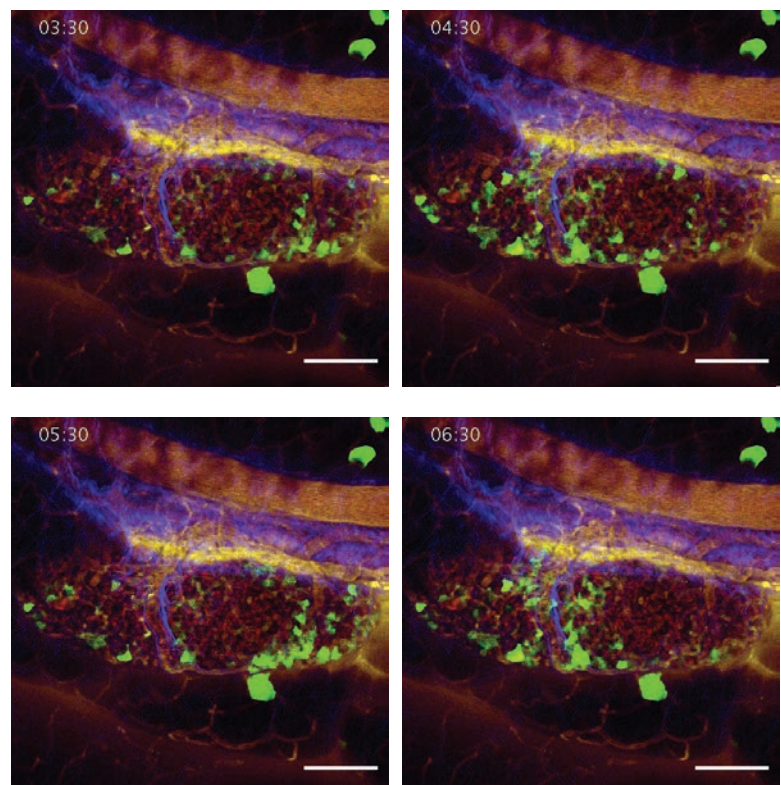


## Supplemental Figure 2

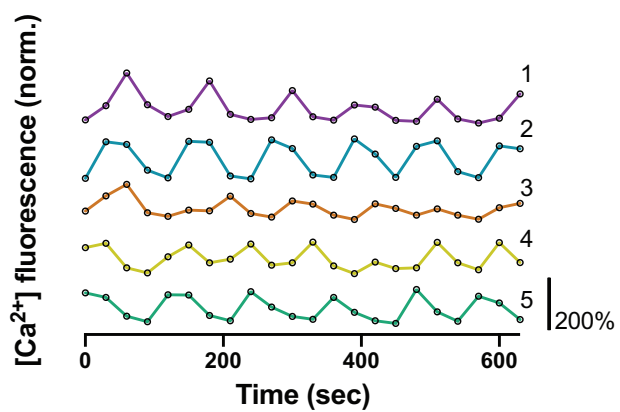
A



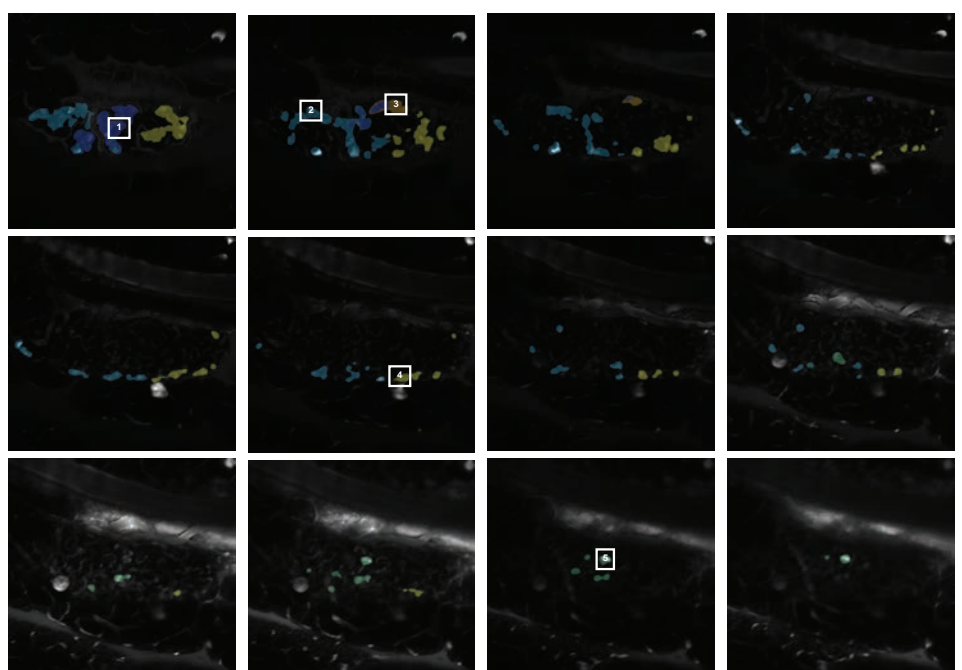
B



C



D





# Supplemental Figure 3

